

Continuous air purification by aqueous interface filtration and absorption

<https://doi.org/10.1038/s41586-022-05124-y>

Received: 6 November 2020

Accepted: 19 July 2022

Published online: 26 September 2022

 Check for updates

Yunmao Zhang¹, Yuhang Han¹, Xiaoliang Ji², Duyang Zang², Long Qiao¹, Zhizhi Sheng^{1,3}, Chunyan Wang¹, Shuli Wang^{1,3}, Miao Wang⁴, Yaqi Hou¹, Xinyu Chen¹ & Xu Hou^{1,3,4,5}✉

The adverse impact of particulate air pollution on human health^{1,2} has prompted the development of purification systems that filter particulates out of air^{3–5}. To maintain performance, the filter units must inevitably be replaced at some point, which requires maintenance, involves costs and generates solid waste^{6,7}. Here we show that an ion-doped conjugated polymer-coated matrix infiltrated with a selected functional liquid enables efficient, continuous and maintenance-free air purification. As the air to be purified moves through the system in the form of bubbles, the functional fluid provides interfaces for filtration and for removal of particulate matter and pollutant molecules from air. Theoretical modelling and experimental results demonstrate that the system exhibits high efficiency and robustness: its one-time air purification efficiency can reach 99.6%, and its dust-holding capacity can reach 950 g m⁻². The system is durable and resistant to fouling and corrosion, and the liquid acting as filter can be reused and adjusted to also enable removal of bacteria or odours. We anticipate that our purification approach will be useful for the development of specialist air purifiers that might prove useful in settings such as hospitals, factories and mines.

Among air pollutants, respirable particles such as PM₁₀, PM_{2.5} and ultrafine particles are of particular concern because their small size allows them to penetrate deep into human bronchi and lungs. Straightforward and effective removal of these fine particles relies on the use of filter units consisting of multilayer fibrous or porous materials with surface treatments to either passively block the motion of solid particles or actively capture pollutants on the filter surface^{8,9}. However, these filter units suffer from fouling issues due to the accumulation of particles on their surfaces and internal pores. As a result, the dust-holding capacity of their surfaces fundamentally limits the efficiency and service life of such filter units¹⁰. Filter units thus need to be regularly replaced or cleaned to maintain optimal performance⁷, with a trade-off between purification efficiency, service life and maintenance cost.

Aqueous interfaces have the ability to capture solid particles after contact¹¹, with particle adhesion from the aqueous environment to gas bubble interfaces extensively studied for applications such as multiphase reactions¹² and flotation processes¹³. However, the opposite effect, so movement of particles from inside gas bubbles to the aqueous interface, has been rarely considered. It forms the basis of our air purification strategy (Fig. 1a) as air moves in the form of bubbles through an ion-doped conjugated polymer-coated matrix infiltrated with a selected functional liquid (the electrochemical liquid-based system (ELBS)).

Principle of ELBS

To exploit the aqueous interfacial absorption of particles from contaminated air, we have created the ELBS that manageably controls

microbubble generation. The purification process of the system is divided into two steps: filtration and absorption. In the filtration process, once contaminated air enters the system, the liquid-filled pores in the matrix act as a coarse filter to perform the filtration process and separate large particles, whereas the liquid lining in the pores prevents particle accumulation on the matrix surface (Fig. 1b). At this stage, a porous matrix with smaller pore sizes will result in a higher purification efficiency and lower air flow. Then, in the absorption process, the small air-borne particles that pass through the porous matrix are trapped inside the microbubbles and continue to move because of inertia and eventually contact the gas–liquid interface (Fig. 1c). The force F_c on the particle promotes capture on the aqueous interface or even drags it into the functional liquid, which is usually an aqueous solution. By efficiently transferring pollutants from air into the aqueous solution, air purification is achieved. The anticlogging property of the liquid-filled pores is further enhanced by turning the wettability of the matrix that influences interactions at the gas–liquid–solid interface¹⁴. Meanwhile, the wettability can be tuned during the purification process using a pulse of positive (oxidation) or negative (reduction) potential.

Commercial filters need to be carefully selected to achieve different purification efficiencies that depend on the required air quality¹⁵. ELBS can also provide a range of purification efficiencies to suit different operating environments by adjusting the size of the generated bubbles. Two approaches can be used to control bubble size: adjusting the pore sizes of the matrix (Fig. 1b) or tuning the wettability of the matrix (Fig. 1c). Smaller bubbles have greater specific surface areas, leading to higher mass transfer rates at gas–liquid interfaces¹⁶. Thus,

¹State Key Laboratory of Physical Chemistry of Solid Surfaces, College of Chemistry and Chemical Engineering, Xiamen University, Xiamen, China. ²Soft Matter & Complex Fluids Group, School of Physical Science and Technology, Northwestern Polytechnical University, Xi'an, China. ³Collaborative Innovation Center of Chemistry for Energy Materials, Xiamen University, Xiamen, China.

⁴Department of Physics, Research Institute for Biomimetics and Soft Matter, Fujian Provincial Key Laboratory for Soft Functional Materials Research, Jiujiang Research Institute, College of Physical Science and Technology, Xiamen University, Xiamen, China. ⁵Innovation Laboratory for Sciences and Technologies of Energy Materials of Fujian Province (IKKEM), Xiamen, China.

✉e-mail: houx@xmu.edu.cn

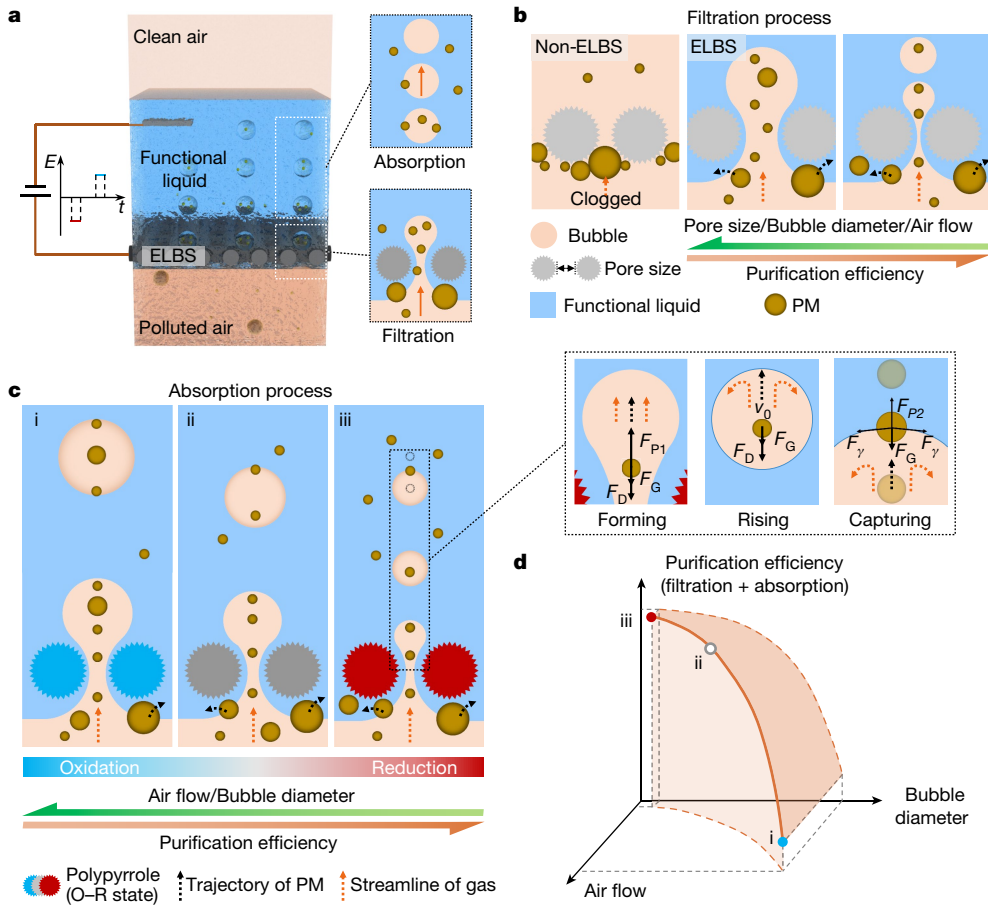


Fig. 1 | Principle and air purification performance of the ELBS. **a**, Schematic illustration of the air purification system. ELBS is composed of a doped conjugated polymer matrix (DPM) and filled with a functional liquid. The purification process integrates two steps: a filtration step and an absorption step. **b**, Schematic sketch of liquid-lined matrix filtration and anticlogging ability. Smaller pores in the matrix lead to smaller bubbles, higher purification efficiency and lower air flux. **c**, Particle absorption process during the bubble-rising stage. The size of microbubbles is regulated by tuning the affinity between the DPM and the functional liquid through the applied redox potential. An oxidation potential leads to larger bubbles and a reduction potential causes smaller bubbles. Tuning of the redox process realizes a range

of purification efficiencies and air flows. The particles move with the air during bubble formation and rise until they touch the gas–liquid interface owing to inertia. When a particle is captured on the gas–liquid interface, the force F_c (the resultant force on the particle) causes it to adhere to the gas–liquid interface or be dragged into the functional liquid. Here, F_{P1} is the force resulting from the pressure difference between the two sides of the pore, F_G is the gravitational force, F_D is the drag force, F_{P2} is the force resulting from the capillary pressure inside the gas bubble, F_γ is the surface tension force of the liquid and v_0 is the velocity of the particle. **d**, Relationships among bubble diameter, air flow and ELBS purification efficiency. The three points correspond to the states presented in **c**.

decreasing the size of air bubbles can enhance the particle separation efficiency for air purification but will impair the air flow rate through the system. Therefore, the trade-off during practical applications among the purification efficiency, the air flow and the bubble diameter can be created (Fig. 1d).

ELBS preparation and filtration process

ELBS is composed of the porous matrix and the functional liquid. The matrix is prepared by interfacial polymerization method to deposit dodecyl benzene sulfonate (DBS⁻) doped polypyrrole (PPy) on stainless-steel mesh (SSM). We utilize the polymerization time and the redox potential to control the pore size and the surface properties of the matrix, respectively (Fig. 2a, Extended Data Fig. 1 and Supplementary Video 1). Then, the LiClO₄ solution was selected as the functional liquid and the interfacial wettability of the matrix can be controllably and reversibly changed owing to Li⁺ ion doping (reduction process, hydrophilic) and dedoping (oxidation process, hydrophobic) in accordance with the applied redox potential (Fig. 2b and Extended Data Fig. 2a). Optimized experimental conditions, composition, surface morphology

and reversible wettability tests are described in the Methods (Extended Data Figs. 2 and 3).

The affinity between the matrix and the functional liquid plays a pronounced role in ELBS filtration process, because the liquid-lined matrix can bring good anti-fouling performance during the filtration process^{17–19}. The surface energy and work of adhesion were calculated to further investigate this affinity (Fig. 2c). The results indicate that reversibly switching the liquid-lined matrix between the steady state and the non-steady state, by regulating the affinity of the functional liquid to the matrix, can be used to prevent particle accumulation (Fig. 2d and Extended Data Fig. 4).

Absorption process

As shown in Fig. 3a, the absorption process of the ELBS is divided into three steps: bubble forming, bubble rising and particle capturing. In the bubble-forming step, we control the size of the generated microbubble by varying the matrix pore size and the redox state of the ELBS (Fig. 3b and Extended Data Fig. 5). With an average pore size of around 9.7 μm, the diameter of the microbubble decreases from around 618 μm

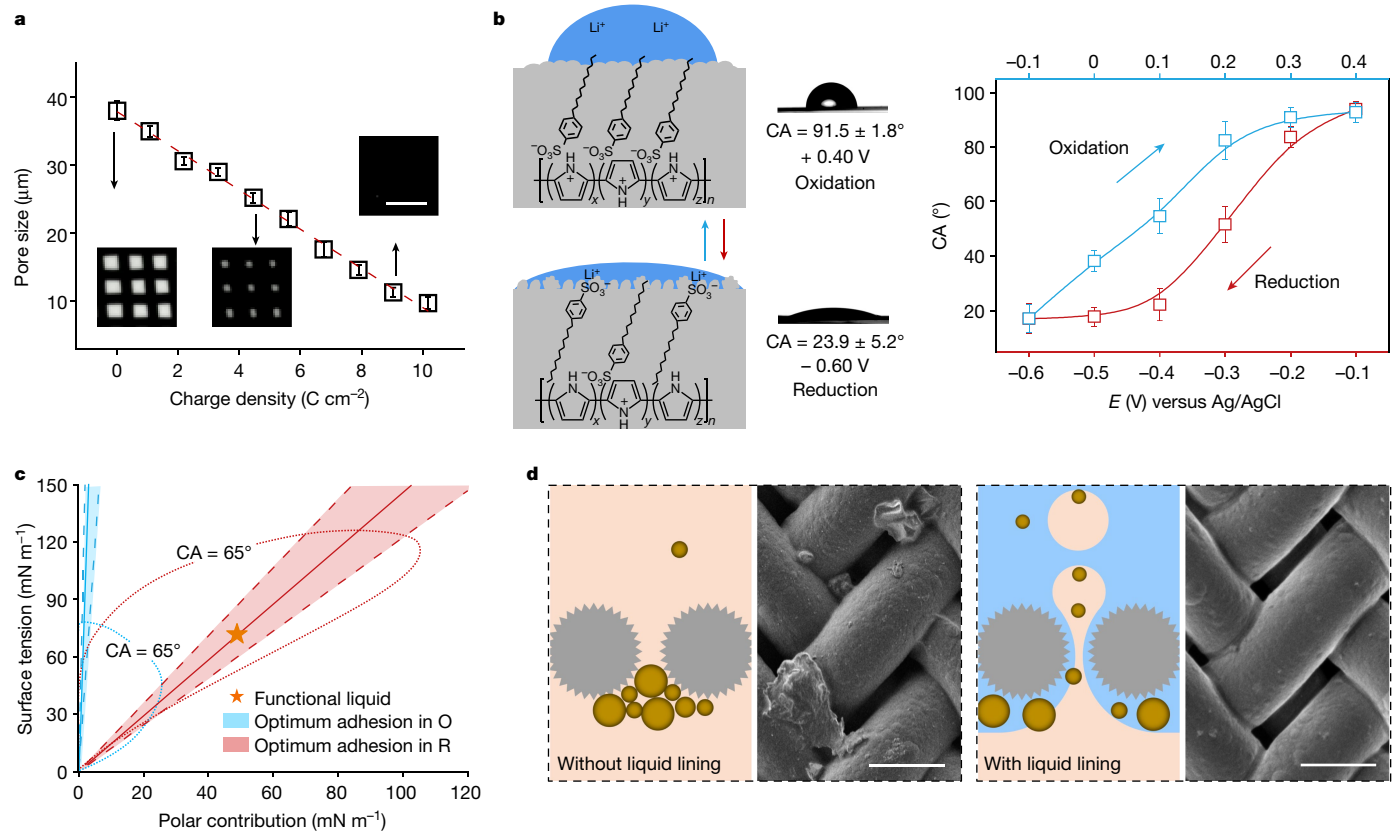


Fig. 2 | Preparation and filtration process of ELBS. **a**, The relationship between pore size of the matrix and charge density. Insets: images of the porous matrix fabricated with different polymerization times. Scale bar, 100 μm . The error bars represent the standard deviation from ten independent pore size measurements. **b**, CA of a LiClO_4 solution drop on the surface of a DPF at different electrochemical potentials. Before applying a reduction or oxidation potential, the DPF was processed into an oxidation state or a reduction state, respectively. During the oxidizing process, the hydrophobic dodecyl chains translate out from the PPy backbone to the surface and Li^+ ions move out of the backbone. When the reduction potential is applied, the hydrophilic sulfonic acid group of the DBS⁻ ions thrust out from the PPy backbone and the Li^+ ions are inlaid into the surface of the matrix. The error bars represent the standard deviation from five independent measurements.

c, Analysis of the adhesion work between the functional liquid and the matrix in oxidation state (O) and reduction state (R), respectively. The polar part of the surface tension/energy and the corresponding surface tension/energy can be identified, and their combination provides the optimum adhesion between the matrix and the functional liquid. The blue and red straight lines represent the optimum adhesive forces and a range of acceptable performances can be proposed. The results indicate that the functional liquid falls in the optimum zone to get a steady state, which means the functional liquid and DPM have good adhesion and affinity in the reduction state. **d**, Anti-fouling performance of ELBS during the filtration process. Scanning electron microscopy images of DPM without liquid lining and DPM from ELBS with liquid lining in the reduction state after the filtration and backwashing. Scale bar, 50 μm .

to approximately 350 μm when the matrix was converted from an oxidation state to a reduction state (Supplementary Video 2). A smaller bubble size provides a much higher particle absorption efficiency (Fig. 3c) because of the more efficient gas–liquid interfacial mass transfer behaviour¹⁶; however, owing to a greater working pressure, smaller bubbles consume more energy (Extended Data Fig. 5c). Therefore, the controllable size range of microbubbles is defined per the application requirement. In our case, the lower limit of the bubble diameter D_{\min} can be calculated as $D_{\min} = L + 2R(1 - \cos \theta)$ from the geometric relationship, in which the centre of the bubble must be higher than the centre of its contact line (Fig. 3b). Here, L is the pore size of the DPM and R is the radius of the fibres of the DPM. The maximum bubble diameter D_{\max} is calculated from the force balance of the bubble, which is derived as $D_{\max} = (6\gamma/\rho_i g L_{1,\max} \sin(\psi_{\max} - \theta))^{1/3}$. In this expression, ψ_{\max} is the texture angle needed to obtain the maximum surface tension force, γ is the surface tension of the functional liquid, ρ_i is the density of the functional liquid, g is the gravity constant, and $L_{1,\max} = L + 2R(1 - \sin \psi_{\max})$ is the corresponding diameter of the contact line of the bubble. Thus, our controllable range of bubble diameter (D_{expt}) values are between D_{\max} and D_{\min} (Extended Data Fig. 5d), which can be tuned by varying the pore size of the matrix and the redox state of the ELBS.

In the bubble-rising step, the key for particles to be trapped by the gas–liquid interface is that they can contact the gas–liquid interface before the bubble bursts (Fig. 3d). The motion of particles in rising bubbles is influenced by several different mechanisms, including convection, gravitational deposition, inertial impaction and Brownian motion²⁰. After theoretical calculating, the stopping distance of most particles is larger than the bubble diameter, which indicates that the particles have enough time to move to the gas–liquid interface before the bubble bursts (Fig. 3d).

In the particle-capturing process, if the particles touch the gas–liquid interface, whether they are hydrophobic or hydrophilic particles, they can be captured by the functional liquids and cannot escape into the gas. In the experiment, when hydrophilic particles touch the gas–liquid interface, the particles quickly adhere to the interface and enter the functional liquid (solution A, LiClO_4) (Fig. 3e and Supplementary Video 3). Hydrophobic particles are quickly captured by the interface but cannot enter the liquid (Extended Data Fig. 6a and Supplementary Video 3). When the solution A is modified by adding sodium DBS (SDBS) to form the solution B, both hydrophilic and hydrophobic particles can rapidly move into the liquid (Fig. 3e and Supplementary Video 3). Thus, most particles can be captured on the gas–liquid interface, and

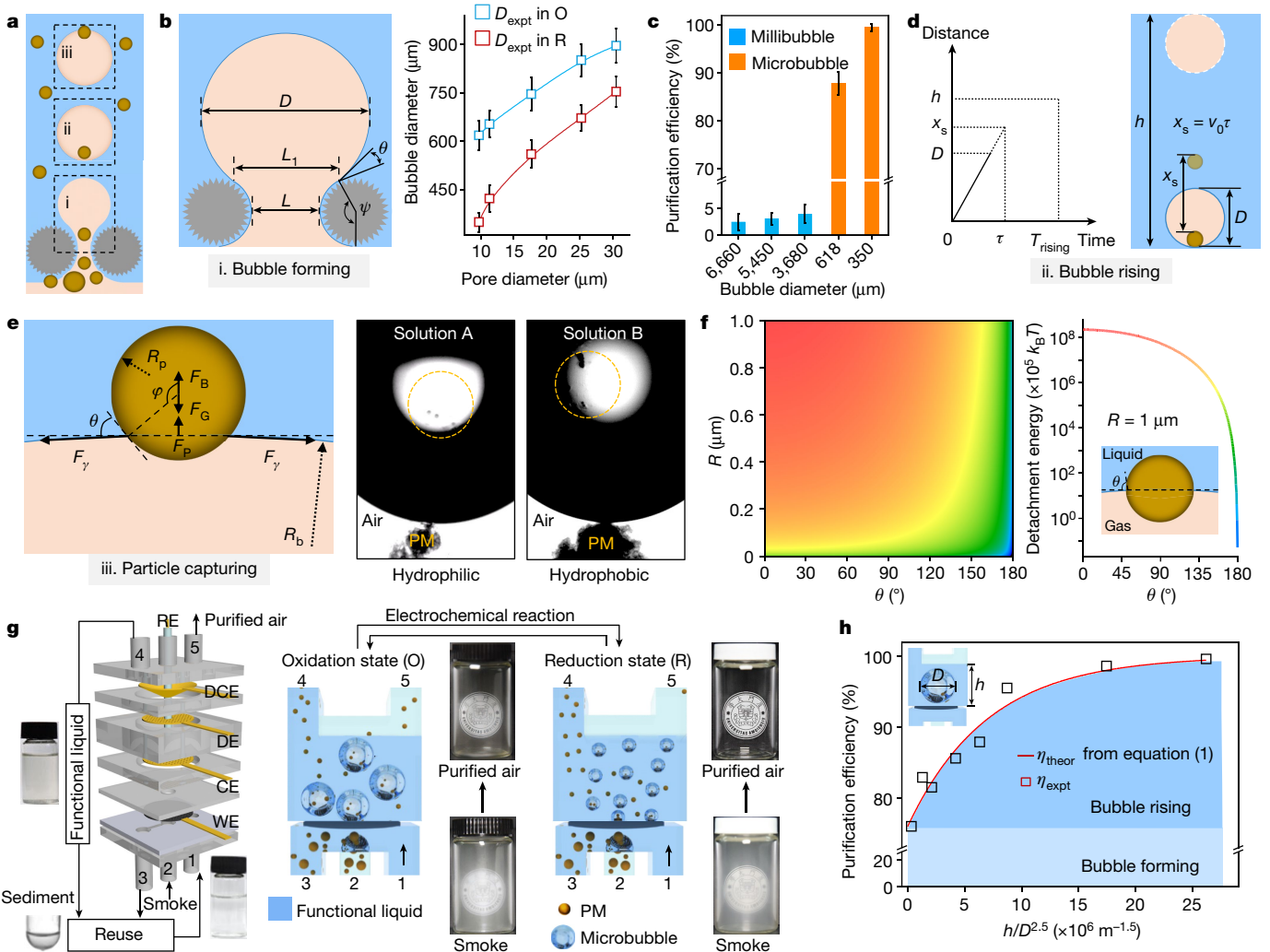


Fig. 3 | Microbubble generation and particle absorption process of the ELBS. **a**, Schematic illustrations of the aqueous interface absorption process. **b**, Left: schematic sketch of a pressure-induced microbubble. Here, D is the diameter of the bubble, L is the pore size of the DPM, L_1 is the diameter of the contact line between the bubble and matrix, θ is the CA and ψ is the texture angle. Right: diameters of microbubbles generated from the ELBS with different matrix pore sizes in different redox states. The error bars represent the standard deviation from five independent measurements. **c**, PM purification efficiency of differently sized bubbles. The error bars represent the standard deviation from five independent measurements. **d**, Distance that particles travel at the initial velocity (v_0) and within the relaxation time (τ) is called the stopping distance (x_s). The particle's stopping distance is larger than the bubble diameter (D) and the relaxation time is smaller than the bubble-rising time, which indicates that the particles will touch the gas–liquid interface during the bubble-rising process. **e**, Left: representation of the forces acting on a particle at the bubble interface. Here, R_p is the radius of the particle, R_b is the radius of the bubble, F_p is the force resulting from the capillary pressure inside the gas bubble, F_B is the buoyancy

force, F_G is the gravitational force and F_γ is the surface tension force of the liquid. Right: both hydrophobic and hydrophilic PM can be captured and can move into the functional liquid by rational design of the ELBS. **f**, Detachment energy of the particle with different CAs for which the radius of the particle is assumed to be 1 μm . **g**, Schematic sketch of an air purification ELBS device (left), which contains four electrodes: DPM as the working electrode (WE), Au/SSM as the counter electrode (CE) and discharge electrode (DE), Ag/AgCl as the reference electrode (RE) and DPM as the droplet collection electrode (DCE). Right: the flow path of functional liquid and smoke and the control process are shown in the cross-sectional view (indicated by the arrows). The functional liquid can be recycled by reprocessing, for example, centrifugation. Demonstration of a hazardous level of smoke in the bottom bottle and the air after ELBS purification in the upper bottle with different redox states. **h**, Theoretical and experimental purification efficiency of the ELBS with different microbubble sizes (D) and functional liquid thicknesses (h). The light blue part is the bubble-forming stage and the blue part is the bubble-rising stage.

whether the particles enter the liquid or not depends on the wettability between the functional liquid and the particle. To further evidence the particle-capture process, we theoretically analyse this capturing process from the viewpoint of energy and force. Once particles contact the gas–liquid interface, on the one hand, according to the surface free energy change (ΔG) of the particle, when the contact angle (CA) is less than 180°, the adhesion of the particle to the gas–liquid interface can occur spontaneously, that is, most particles can be trapped by the liquid because their CAs are less than 180° (ref. ²¹). On the other hand,

the resultant force on a particle determines its moving direction, and this force depends on the particle wettability; when the CA is greater than 90°, most of the volume of the particle is on the gas side; if the CA is less than 90°, the particle tends to move into the liquid (Fig. 3e and Extended Data Fig. 6b). Furthermore, we interpreted the energy required for particles to detach from the interface into the gas as $W = \gamma_0 R_p^2 \pi (1 + \cos\theta)^2$ (ref. ²²), where γ_0 is the interfacial tension and R_p is the particle radius. As shown in Fig. 3f, the detachment energy increases significantly when the CA is less than 180°. For example, if

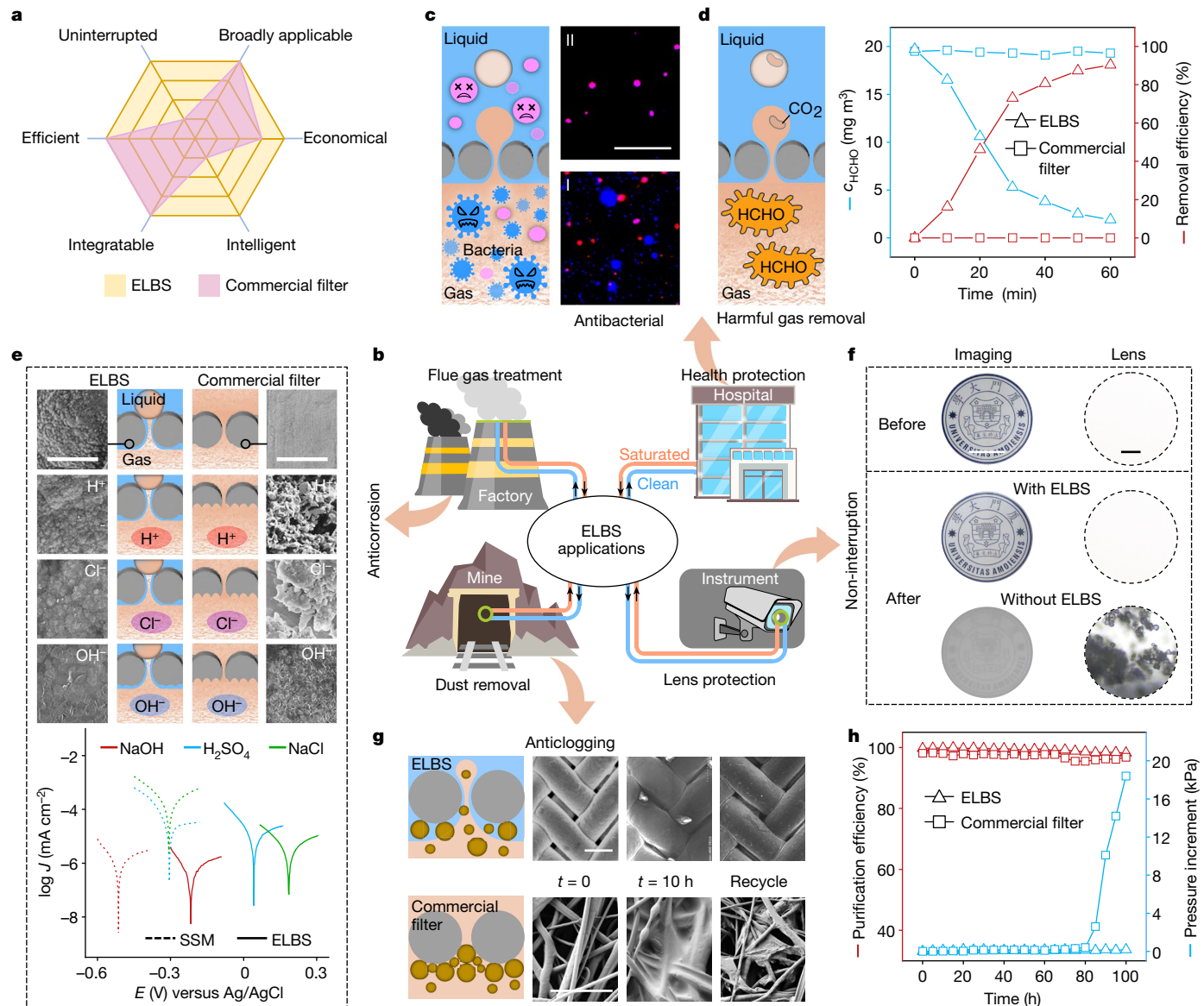


Fig. 4 | Applications and performance of ELBS. **a**, Radar chart of the capabilities of air purification strategies. As shown in pink, commercial filters with high efficiency can be installed in a variety of places. However, these filters are easily blocked in certain environments and need to be replaced manually, interrupting filter function. The ELBS with liquid material as an adsorbent can effectively solve some core issues of commercial filters that use solid fibres, as shown in yellow. **b**, Application scenario display. The blue and orange lines represent pipelines that transport clean and contaminant-absorbing functional liquids, respectively. **c**, Antibacterial performance of the ELBS. In fluorescence micrographs of bacteria, live cells are stained blue, whereas dead cells are stained magenta: I, functional liquid without antibiotic; II, functional liquid with antibiotic. Scale bar, 50 μ m. **d**, Formaldehyde removal test of the ELBS and commercial melt-blown filters. The concentration of formaldehyde decreases

rapidly when using the ELBS, whereas it does not change significantly when using the melt-blown filters. **e**, SEM images of the DPM from the ELBS and the SSM before and after exposure to 1.0 M NaOH, 1.0 M NaCl and 0.5 M H₂SO₄ at 80 °C for 24 h. Scale bar, 1 μ m. Bottom: potentiodynamic polarization curves of the DPM from the ELBS and the bare SSM in 1.0 M NaOH, 1.0 M NaCl and 0.5 M H₂SO₄ at room temperature. **f**, Protective tests of a camera lens with and without the ELBS. When using the ELBS, clean air sweeps the lens surface, reducing particle aggregation and keeping the camera image clear. Scale bar: white, 4 cm; black, 50 μ m. **g**, SEM images of the DPM from the ELBS and melt-blown filters after filtration and backwashing. Scale bar, 50 μ m. **h**, Long-term PM purification efficiency and applied pressure change of the ELBS and a commercial melt-blown filter under a continuous hazardous level of PM pollution.

the radius of the particles is 1 μ m and the CA is 150°, the detachment energy is about $1 \times 10^6 k_B T$, which shows that even super-hydrophobic particles will also be strongly held in the interface. Therefore, the ELBS can capture both hydrophobic and hydrophilic particles and show ideal purification efficiency.

The air purification performance of the ELBS was further investigated (Fig. 3g, Extended Data Fig. 6e and Supplementary Video 4). The functional liquid can be reused after processing, such as after centrifugation and catalytic decomposition. We can adjust the redox

state to obtain the required air flow at a desired air purification efficiency. The bubble forming (filtration process) and bubble rising (absorption process) is considered to determine the ultimate purification efficiency (Fig. 3h). From a quantitative point of view, we hypothesized that the absorption amount Γ_t of particulate matter (PM) crossing a unit area in a unit time is proportional to the particle concentration c_t in the microbubble; that is, $\Gamma_t = kc_t$, where k is the total absorption coefficient. The efficiency η of a single bubble can be expressed as:

$$\eta = 1 - \left(1 - \frac{\Delta W_1}{W_0}\right) \exp\left(-41.59 \frac{\mu_1^{2/3}}{g^{5/6} \rho_1^{2/3}} k \frac{h}{D^{5/2}}\right) \quad (1)$$

where ΔW_1 is the reduction in PM in the bubble-forming stage, W_0 is the initial amount of PM in the polluted air, μ_1 is the viscosity of the functional liquid, D is the microbubble diameter and h is the thickness of the functional liquid. In our case, we obtain the theoretical efficiency during the bubble-forming stage $\Delta W_1/W_0$ (76.0%) and k ($2.3 \times 10^{-4} \text{ m s}^{-1}$) by fitting equation (1) to the experimental results (Fig. 3h and Extended Data Table 3). Then, the efficiency η can be simplified as: $\eta = 1 - 0.24 \exp\left(-1.43 \times 10^{-7} \frac{h}{D^{5/2}}\right)$, which indicates that, for a certain ELBS, the air purification efficiency is only related to the bubble diameter and the thickness of the functional liquid. The total air purification efficiency is higher with a smaller bubble and a thicker functional liquid because of the large interphase mass transfer rate and the long rising time for mass transfer in the bubble-rising stage²³. Therefore, we can improve the ultimate purification efficiency by regulating the redox state of the ELBS and adjusting the thickness of the functional liquid.

Applications

Commercial filters are widely used in air purification equipment, but can face issues such as fouling, clogging, frequent filter replacement and so on. (Fig. 4a)^{7,24,25}. The ELBS allows for continuous, programmable and automated purification without being affected by corrosion or clogging, which is attractive for applications including health protection, flue gas treatment and dust removal (Fig. 4b). Because the functional liquid can be adjusted, the ELBS can be tuned to the performance characteristics required for particular purification needs, such as antibacterial ability (Fig. 4c) or the removal of odours and hazardous air pollutants (Fig. 4d). The proof-of-concept test with formaldehyde²⁶ illustrates that the ELBS has good removal performance, although we note that odour and other gas-phase pollutant removal requires the matching of the functional liquid to the specific pollutant molecule to be removed. The development of more generally and widely applicable functional fluids needs to be explored.

Chemical corrosion challenges air purification equipment under harsh conditions during flue gas treatment²⁷. The ELBS can not only remove corrosive flue gases, but also has a good corrosion resistance (Fig. 4e). The characterization of material surface topography shows that the surface of a bare SSM was heavily corroded, whereas the surface of the DPM from the ELBS remained almost unchanged, indicating the anticorrosion properties of the ELBS (Fig. 4e, top and Extended Data Fig. 7). The corrosion potential E_{corr} and the corrosion current density J_{corr} provide further evidence of the good anticorrosion properties (Fig. 4e, bottom).

A particularly promising application scenario of the ELBS is for instrument maintenance in heavily polluted environments^{28,29}, such as for maintaining surveillance cameras that constitute an important prevention measure in hazardous environments such as mines and factories. Under the above working conditions, the lenses of cameras are easily contaminated by particles in a highly polluted environment. The ELBS tackles this problem and enables continuous purification to ensure safe monitoring (Fig. 4f).

The ELBS offers long-term stable performance at low cost because of its inherent anticlogging properties. The liquid-based material strategy will reduce the consumption of solid filtration materials and promote the possibility of permanent application without the need for replacing filters. As shown in Fig. 4g, the porous matrix of the ELBS can be easily cleaned by backwashing. Compared with the commercial filter, after operation for over 100 h under a hazardous environment, the ELBS show better anticlogging performance and maintains a 98.2% purification efficiency with no noticeable increase in the applied pressure (Fig. 4h).

The durability and dust-holding capacity are two other important features of air purification systems³⁰, and the ELBS with a high purification efficiency of 99.6% stands out in view of its large dust-holding capacity of 950 g m^{-2} , which is five to ten times higher than that of other purification systems (Extended Data Table 4).

Discussion

The ELBS is promising for continuous air purification as it integrates two steps: the direct interception and removal of larger PM in polluted air by a liquid-lined porous matrix, and the capture of smaller PM by a functional liquid through the microbubble interface. The liquid, as both a structural and functional material in the ELBS, can be reused to achieve long-term stability and can be designed to extend its functionality with antibacterial or hazardous gas removal properties. The purification efficiency can be rationally tuned by electrochemical regulation of the size of the generated microbubbles and the thickness control of the functional liquid. Coupling theoretical modelling with experimental demonstrations sheds light on the mechanisms of controllable microbubble generation and particle capture at the aqueous interface. We envisage that coupling our system with smart, artificial intelligence-based microfluidic and liquid gating technology might enable rapid regulation of the ELBS functional liquids to meet the air purification needs in changing and challenging environments.

Online content

Any methods, additional references, Nature Research reporting summaries, source data, extended data, supplementary information, acknowledgements, peer review information; details of author contributions and competing interests; and statements of data and code availability are available at <https://doi.org/10.1038/s41586-022-05124-y>.

- Nel, A. Air pollution-related illness: effects of particles. *Science* **308**, 804–806 (2005).
- Dedoussi, I. C., Eastham, S. D., Monier, E. & Barrett, S. R. H. Premature mortality related to United States cross-state air pollution. *Nature* **578**, 261–265 (2020).
- Stanford, M. G. et al. Self-sterilizing laser-induced graphene bacterial air filter. *ACS Nano* **13**, 11912–11920 (2019).
- Zhang, G. H. et al. High-performance particulate matter including nanoscale particle removal by a self-powered air filter. *Nat. Commun.* **11**, 1653 (2020).
- Wang, Q. et al. Polarity-dominated stable N97 respirators for airborne virus capture based on nanofibrous membranes. *Angew. Chem. Int. Ed.* **60**, 23756–23762 (2021).
- Zhang, Y. et al. Preparation of nanofibrous metal-organic framework filters for efficient air pollution control. *J. Am. Chem. Soc.* **138**, 5785–5788 (2016).
- Liu, G. L. et al. A review of air filtration technologies for sustainable and healthy building ventilation. *Sustain. Cities Soc.* **32**, 375–396 (2017).
- Liu, C. et al. Transparent air filter for high-efficiency PM2.5 capture. *Nat. Commun.* **6**, 6205 (2015).
- Li, M. et al. Novel hollow fiber air filters for the removal of ultrafine particles in PM2.5 with repetitive usage capability. *Environ. Sci. Technol.* **51**, 10041–10049 (2017).
- Zhong, Z. et al. Unusual air filters with ultrahigh efficiency and antibacterial functionality enabled by ZnO nanorods. *ACS Appl. Mater. Interfaces* **7**, 21538–21544 (2015).
- Omota, F., Dimian, A. C. & Bliek, A. Adhesion of solid particles to gas bubbles. Part 1: modelling. *Chem. Eng. Sci.* **61**, 823–834 (2006).
- Dedoussi, D. et al. Multiphase microreactors based on liquid-liquid and gas-liquid dispersions stabilized by colloidal catalytic particles. *Angew. Chem. Int. Ed.* **60**, 2–25 (2022).
- Zhang, M. & Guiraud, P. Surface-modified microbubbles (colloidal gas aphrons) for nanoparticle removal in a continuous bubble generation-flotation separation system. *Water Res.* **126**, 399–410 (2017).
- Wesley, D. J., Smith, R. M., Zimmerman, W. B. & Howse, J. R. Influence of surface wettability on microbubble formation. *Langmuir* **32**, 1269–1278 (2016).
- Brown, K. L. & Wray, S. In *Hygiene in Food Processing* (eds Lelieveld, H. L. M., Holah, J. T. & Napper, D.) 174–202 (Woodhead Publishing, 2014).
- Agarwal, A., Ng, W. J. & Liu, Y. Principle and applications of microbubble and nanobubble technology for water treatment. *Chemosphere* **84**, 1175–1180 (2011).
- Hou, X., Hu, Y., Grinthal, A., Khan, M. & Aizenberg, J. Liquid-based gating mechanism with tunable multiphase selectivity and antifouling behaviour. *Nature* **519**, 70–73 (2015).
- Alvarenga, J. et al. Research Update: Liquid gated membrane filtration performance with inorganic particle suspensions. *APL Mater.* **6**, 100703 (2018).
- Mao, X. W. et al. Energetically efficient electrochemically tunable affinity separation using multicomponent polymeric nanostructures for water treatment. *Energ. Environ. Sci.* **11**, 2954–2963 (2018).
- Pich, J. & Schutz, W. On the theory of particle deposition in rising gas-bubbles: the absorption minimum. *J. Aerosol Sci.* **22**, 267–272 (1991).

Article

21. Wei, Y., Zhang, Q. & Thompson, J. E. The wetting behavior of fresh and aged soot studied through contact angle measurements. *Atmos. Clim. Sci.* **7**, 11–22 (2017).
22. Binks, B. P. & Lumsdon, S. Influence of particle wettability on the type and stability of surfactant-free emulsions. *Langmuir* **16**, 8622–8631 (2000).
23. Kumar, B., Patil, A. J. & Mann, S. Enzyme-powered motility in buoyant organoclay/DNA protocells. *Nat. Chem.* **10**, 1154–1163 (2018).
24. Li, P. et al. Metal-organic frameworks with photocatalytic bactericidal activity for integrated air cleaning. *Nat. Commun.* **10**, 2177 (2019).
25. Tian, E. et al. Ultralow resistance two-stage electrostatically assisted air filtration by polydopamine coated PET coarse filter. *Small* **17**, e2102051 (2021).
26. Xiao, R., Mo, J., Zhang, Y. & Gao, D. An in-situ thermally regenerated air purifier for indoor formaldehyde removal. *Indoor Air* **28**, 266–275 (2018).
27. Lu, W. et al. Polyamine-tethered porous polymer networks for carbon dioxide capture from flue gas. *Angew. Chem. Int. Ed.* **51**, 7480–7484 (2012).
28. Van Harmelen, A., Kok, H. & Visschedijk, A. *Potentials and Costs to Reduce PM10 and PM2.5 Emissions from Industrial Sources in the Netherlands* (TNO Environment, Energy and Process Innovation, 2002).
29. Chen, L., Li, P., Liu, G., Cheng, W. & Liu, Z. Development of cement dust suppression technology during shotcrete in mine of China – a review. *J. Loss Prev. Process Ind.* **55**, 232–242 (2018).
30. Zhu, M. M. et al. Electrospun nanofibers membranes for effective air filtration. *Macromol. Mater. Eng.* **302**, 1600353 (2017).

Publisher's note Springer Nature remains neutral with regard to jurisdictional claims in published maps and institutional affiliations.

Springer Nature or its licensor holds exclusive rights to this article under a publishing agreement with the author(s) or other rightsholder(s); author self-archiving of the accepted manuscript version of this article is solely governed by the terms of such publishing agreement and applicable law.

© The Author(s), under exclusive licence to Springer Nature Limited 2022

Methods

Materials

SDBS, dichloromethane and formaldehyde were purchased from Sinopharm Chemical Reagent Co., Ltd. Pyrrole, LiClO₄, KMnO₄, H₂SO₄, nanofumed silica (hydrophobic-260 and hydrophilic-300), ethylene glycol and diiodomethane were purchased from Aladdin Reagent Inc. AISI 304 austenitic stainless steel mesh (SSM) was purchased from Shijiazhuang Hangxu Metal Products Co., Ltd. Smooth AISI 304 austenitic stainless steel plate (SSP) was purchased from Dongtai Penglian Stainless-steel Products Co., Ltd. All chemicals were of analytical reagent grade and were used as received. Milli-Q deionized water with a resistivity of 18.2 MΩ cm was used.

Materials characterization

Cyclic voltammetry measurement of the DPM was carried out in 0.1 M LiClO₄ aqueous solution. The redox process of the DPM was carried out at different potentials in 0.1 M LiClO₄ aqueous solution. The scanning electron microscope (SEM) images of the DPM were obtained by field-emission scanning electron microscopes Hitachi s-4800 (Hitachi, Japan) and Zeiss GeminiSEM 500 (Carl Zeiss Corp., Germany). X-ray photoelectron spectroscopy analyses were carried out by Thermo Fisher K-alpha (Thermo Fisher Scientific Inc.). CAs and surface tension measurements were conducted on an OCA100 machine (Data Physics, Germany) at ambient temperature. The liquid drops (3 μl) were dropped onto the doped PPy plane film (DPF) under different redox states. The values of the CAs and surface tensions were an average of five independent measurements. Atomic force microscopy images were acquired using a Cypher S atomic force microscope (Asylum Research/Oxford Instruments) in the tapping mode at ambient conditions. The particle size distribution in the functional liquid was studied by dynamic light scattering using a Nanopartica SZ-100 (HORIBA Ltd, Japan).

Synthesis

All electrochemical synthesis and measurements were carried out on a CHI 660 E Electrochemical workstation (CH Instrument Inc.). The dodecyl benzene sulfonate anion doped PPy coated SSM (DPM) was synthesized by a electrochemical polymerization method³¹. Owing to the large diameter error of the local pores of the SSM, it is necessary to pre-select a more uniform part of the pore size for polymerization. Before polymerization, Au was deposited on the SSM by ion sputtering under 8 mA for 60 s using an ion sputter SBC-12 (KYKY Technology Co., Ltd). A three-electrode system was used to control the electrochemical polymerization. Au-coated SSM (Au/SSM) was served as the working electrode. A Ag/AgCl electrode and a platinum plate were used as the reference electrode and the counter electrode, respectively. The electrochemical polymerization was conducted at a constant potential (0.8 V versus Ag/AgCl) in an aqueous solution containing 0.1 M pyrrole and 0.1 M SDBS. The controllable pore size of the DPM was obtained by electrochemical polymerization for various times. To avoid the influence of structure on the CA, a smooth SSP was selected as another substrate for doped PPy polymerization, and this doped PPy plane film was called the DPF.

Critical pressure measurements

The transmembrane properties of the ELBS were determined by measuring the critical pressure (P_c) during the flow of gas. P_c was measured by a wet/wet current output pressure transmitter PX273-02ODI (OMEGA Engineering Inc.). A Harvard Apparatus PHD ULTRA syringe pump with a flow rate of 2,000 μl min⁻¹ was used in the experiments. The DPM with 0.1 M LiClO₄ aqueous solution added was placed in the self-designed electrochemical pressure measurement setup as shown in Extended Data Fig. 5a. The redox process of the DPM from the ELBS was carried out in the setup. The DPM served as the working electrode. A Ag/AgCl electrode and a platinum plate with a hole in the middle were used

as the reference electrode and the counter electrode, respectively. A negative (-0.6 V versus Ag/AgCl) or a positive potential (+0.4 V versus Ag/AgCl) was applied during the measurement to control the redox state. After the reduction or the oxidation, the next P_c measurement was carried out.

Controllable microbubble generation

This was carried out by passing compressed air through the ELBS, with the constant pressure controlled by a Harvard Apparatus PHD ULTRA syringe pump. The DPM was the working electrode, the Au/SSM was the counter electrode, the Ag/AgCl was the reference electrode and the LiClO₄ aqueous solution was the functional liquid. High-speed video was captured using a FASTCAM Mini AX100 camera (Photron) at a resolution of around 1,024 × 1,024 pixels and frame rates of around 1,000 fps. The arithmetic mean was then taken of the bubbles imaged throughout the data set. The pressure was measured by a wet/wet current output pressure transmitter PX273-02ODI (OMEGA Engineering Inc.). The applied pressure was about 1.5 times the critical pressure in the reduction state and the channel diameter of the gas passage was 4 mm.

Adhesion of particles to the gas–liquid interface

Adhesion experiments of the particles to the gas–liquid interface were carried out on a OCA100 machine (Data Physics). A small liquid drop formed at the top of a needle approaches the solid particles to capture particles from the holder. Video images recorded with a charged coupled device camera on the OCA100 machine enabled us to observe the particles adhering to the liquid drop. Here we used nanofumed silica (hydrophobic-260 and hydrophilic-300) as demo particles. Then 0.1 M LiClO₄ aqueous solution and 0.1 M LiClO₄ + 0.05 M SDBS aqueous solution were used as solution A and solution B, respectively.

PM generation and efficiency measurement

For all performance tests, PM was generated from cigarette smoke by burning. The smoke particles had a wide size distribution from less than 50 nm to more than 10 μm⁴. The inflow concentration was controlled by diluting the smoke PM by air to a hazardous pollution level equivalent to a PM_{2.5} index of more than 250 μg m⁻³ and the number of PM (>0.3 μm) particles of more than 3 × 10⁵ l⁻¹. PM number concentrations were detected with and without the ELBS using a laser particle counter PM 5003S (Plantower) and the purification efficiency was calculated by comparing the concentration before and after purification. To ensure the precision and consistency of the sensor, the sensor was calibrated with a DustTrak 8530 and Laser Aerosol Spectrometer 3340 (TSI Inc.).

Air purification measurement

The setup for in situ air purification measurement is displayed in Fig. 3g and Extended Data Fig. 6c,d. The DPM with 0.1 M LiClO₄ aqueous solution added was placed in the setup. The DPM served as the working electrode. The Ag/AgCl electrode and the Au/SSM with a hole in the middle were used as the reference electrode and the counter electrode, respectively. A conductive polymer electrode was added as the droplet collection electrode on the outlet side to capture the droplet generated from the bursting bubbles by electrostatic interactions. The counter electrode was also used to form an electric field between these two electrodes. There was a bulge in the centre of the collector electrode and the droplets were collected spontaneously owing to gravity and did not stay on the surface, avoiding secondary contamination. The polluted air entered from the bottom of the setup and the functional liquid entered in a direction perpendicular to the air. The functional liquid was divided into two parts on the matrix: one part flowed with the air across the matrix, and the other part flowed at the bottom of the matrix. The purified air and the liquid that had absorbed the pollutants flowed out from the upper part of the device, and then the liquid was sent for recycling. After the reduction or the oxidation, the air

Article

purification process and measurement were carried out. During the long-term purification test, a rapid cleaning process was performed on the ELBS every ten hours, in which the functional liquid flowed back through the DPM to remove any large particles. The dust-holding capacity of the ELBS was calculated from the mass of absorbed particles for 100 h. Five-layer melt-blown filters (Henan Piaoan Group Co., Ltd) were tested in the same way without the functional liquid.

Antibacterial activity of the ELBS

Gram-negative *Escherichia coli* (ATCC25922) was used to reveal the antibacterial activity of the ELBS. The bacterial strain was first proliferated in lysogeny broth (LB, EMD Millipore Corporation) medium at 37 °C for 12 h. Then, bacterial cells were collected by centrifuging a 1 ml mixture mentioned above (4,000 r.p.m. at 4 °C for 10 min) and then they were resuspended in sterile saline solution (0.85% (w/v)). A 10% functional liquid in LB medium (v/v) with 50 µg ml⁻¹ gentamicin (Shanghai Basal Media Technologies Co., Ltd) was used as an experimental group. A 10% functional liquid in LB medium (v/v) without gentamicin was used as a control. All the groups (each with triplicated samples) were added with the same 1% resuspended *Escherichia coli* solution mentioned above and incubated in an orbital shaker at 37 °C at 150 r.p.m. for 6 h. The antibacterial activity was measured by using an Apoptosis and Necrosis Assay Kit (Beyotime Institute of Biotechnology). In brief, cells were washed twice with phosphate-buffered saline (pH 7.4), and 100 µl of the cell suspension was transferred to black 48-well plates. The cells were then stained with Hoechst 33342 (10 ng ml⁻¹) and propidium iodide (10 ng ml⁻¹) for 20 min at 4 °C in the dark. The condensed or fragmented nuclei of the apoptotic cells were observed using a Olympus IX73 fluorescence microscope (Olympus Corporation).

Anticorrosion test

The DPM of the ELBS, the SSP and the SSM were immersed in 1.0 M NaOH, 0.5 M H₂SO₄ and 1.0 M NaCl solutions, respectively, at different temperatures for 24 h. To quantitatively characterize the corrosion rates of the materials, electrochemical measurements were conducted with a standard three-electrode configuration in a 1.0 M NaOH, 0.5 M H₂SO₄ and 1.0 M NaCl solutions, at room temperature, respectively. In all measurements, the material mentioned above was used as the working electrode, a platinum plate was used as the counter electrode, Ag/AgCl was used as the reference electrode and the scanning rate was fixed at 1 mV s⁻¹.

Formaldehyde removal test of the ELBS

A 0.1 M KMnO₄ and 0.05 M H₂SO₄ aqueous solution was selected as the functional liquid. Then the ELBS was put into a 1 l chamber in which the formaldehyde concentration was about 20 mg m⁻³. The concentration was measured by the Formaldemeter htV (PPM Technology Ltd). Polluted air entered the ELBS at a rate of 1 l min⁻¹ through a peristaltic pump LabV6 (Shenchen).

The camera lens and its imaging protection

A CS-CP1-1C2WFR camera (EZVIZ Inc.) was put in a chamber at a hazardous dust level. The ELBS was installed before the lens to allow the clean air stream to blow towards the lens surface. Then the images produced by the camera were recorded.

Evaluation of the surface energy

The forces generated when a liquid comes into contact with a solid are theoretically described by Young's equation³²:

$$\gamma_s = \gamma_{sl} + \gamma_l \cos\theta \quad (S1)$$

where θ is the CA between the liquid and the solid, and γ_s , γ_l and γ_{sl} represent the surface energy of the solid, the surface tension of the liquid and the interfacial energy between the liquid drop and the solid,

respectively. According to the Owens–Wendt–Rabel–Kaelble method, which describes the polar and disperse components of the surface energy, the CA between a liquid and a solid surface with their corresponding surface energies can be expressed as (where p denotes polar and d disperse)³³:

$$\frac{1}{2}(1 + \cos\theta) \frac{\gamma_l}{\sqrt{\gamma_l^d}} = \sqrt{\gamma_s^p} \sqrt{\frac{\gamma_l^p}{\gamma_l^d}} + \sqrt{\gamma_s^d} \quad (S2)$$

After the CA measurement, the surface energy and the polar and dispersive components of the PPy plane film (DPF) were calculated using surface energy calculation software with the Owens–Wendt–Rabel–Kaelble method (Data Physics). For the surface properties of the liquids, refer to refs.^{34,35}. The results are that: the total surface energy of the DPF is 39.5 mN m⁻¹ in oxidation state and 63.9 mN m⁻¹ in reduction state; the polar component of the total surface energy of the DPF is 0.8 mN m⁻¹ in the oxidation state and 43.8 mN m⁻¹ in the reduction state; and the dispersive component of the total surface energy of the DPF is 38.7 mN m⁻¹ in the oxidation state and 20.1 mN m⁻¹ in the reduction state.

Derivation of the critical pressure P_c

We measured and derived the critical pressure (P_c) for air passing through the ELBS (Extended Data Fig. 5a), which is the minimum pressure required to form bubbles and a key parameter of bubble generation. Theoretically, we apply a gas pressure P_a and continuously increase it to deform the gas–liquid interface so that it advances upwards along the inner surface of the porous matrix (Extended Data Fig. 5b). Consider a liquid in the Wenzel state³⁶ on a textured surface composed of periodic, cylindrical fibres with radius R and interfibre spacing L . The liquid–air interface with a CA θ is located at a local texture angle ψ , which is the angle between the line connecting the fibre centres and the liquid–solid tangent line. A force balance between the external force caused by the applied pressure P_a on the interface and the force from the surface tension can be written as

$$P_a \times (\text{forced area}) = \gamma \times (\text{contact line length}) \times \sin(\psi - \theta) \quad (S3)$$

For the side length of the square hole of $2(L/2 + R - R\sin\psi)$, equation S3 becomes

$$P_a \times 4 \times (L/2 + R - R\sin\psi)^2 = \gamma \times 8 \times (L/2 + R - R\sin\psi) \times \sin(\psi - \theta) \quad (S4)$$

Simplifying equation S4, we get

$$P_a = \frac{2\gamma \sin(\psi - \theta)}{L/2 + R - R\sin\psi} \quad (S5)$$

For the given liquid and the re-entrant texture geometry, equation S5 indicates that the applied pressure P_a has a relationship with the local texture angle ψ . We determine the critical texture angle ψ_{cr} , which corresponds to the maximum pressure P_c as

$$\frac{dP_a}{d\psi} = 0 \text{ with } \frac{d^2P_a}{d\psi^2} < 0 \text{ at } \psi = \psi_{cr} \quad (S6)$$

From equations S5 and S6 we obtain the critical texture angle

$$\psi_{cr} = \theta + \cos^{-1}\left(\frac{R\sin\theta}{R + L/2}\right) \quad (S7)$$

The gas–liquid interface continues to bend until it approaches ψ_{cr} . The value of ψ_{cr} then corresponds to the location where the gas–liquid interfacial tension can hold the critical pressure P_c , which is

$$P_c = \frac{2\gamma \sin(\psi - \theta)}{L/2 + R - R \sin \psi} \quad (S8)$$

When $P_a > P_c$, the liquid–air interface spontaneously advances upwards and the liquid interaction between the interface and texture transitions to the Cassie–Baxter state. The surface tension of the 0.1 M LiClO₄ aqueous solution is 71.15 mN m⁻¹ and the value of $(R + L/2)$ is 34.3 μm. The data of Young's CA θ in equation S7 is tested on the PPy plane film (not the PPy; see Synthesis section). The CA on the doped PPy coated stainless-steel mesh (DPM) will be influenced by the textured surface. The doped PPy plane film (DPF) is polymerized on a smooth stainless-steel plate to avoid the influence of structure on the CA. The angles θ are about 91.5° and 23.9° in the oxidation and reduction states, respectively. This derivation relationship predicts P_c for air to flow through the ELBS with different pore sizes and redox states and allows us to quantitatively determine how the performance of the ELBS depends on pore size, redox state and liquid properties.

Derivation of the microbubble diameter

When the applied pressure P_a of the gas reaches P_c , the gas–liquid interface continues to bend along the cylindrical geometry fibre and advance upwards until it forms a bubble (Fig. 3b). In the initial stage, the bubble grows and its curvature centre will exceed the centre of the three-phase contact line. From the simple geometric relationship, the centre of the bubble must be higher than the centre of its contact line. Thus, the lower limit of the bubble diameter can be calculated as $D_{\min} = L + 2R(1 - \cos\theta)$. When the bubble detaches from the DPM, the diameter of the bubble will not change significantly. For a precise prediction, it is critical to determine the moment when the bubble is detached from the DPM. Mathematical models developed by balancing the forces acting on the bubble can be used to depict the evolving process of the previously mentioned bubble. It is found that the forces, such as the inertia force F_I , the drag force (viscous force) F_D , the air momentum force F_M , the surface tension force F_γ and the buoyancy force F_B exist during the whole bubble-formation process³⁷. In the initial stage, buoyancy drives the bubble upwards, whereas the surface tension force and the viscous force exerted by the surrounding fluid together counteract buoyancy and delay the detachment of the bubble from the substrate. The high-velocity air also has momentum force and its direction is consistent with the buoyancy. The inertia force is due to the expansion of the bubble at a corresponding speed, and its direction is consistent with the drag force. The gravity force of the bubble is ignored here because it is negligible compared to the buoyancy force. These forces can be divided into detaching forces and attaching forces according to their effect on the bubble. The forces are expressed as follows³⁷:

$$F_B = \frac{1}{6}\pi D^3 \rho_g g \quad (S9)$$

$$F_M = \frac{\pi}{4} L^2 \rho_g u_g^2 \quad (S10)$$

$$F_I = \frac{d}{dt} [u_b V_b (\rho_g + C_{MC} \rho_l)] \quad (S11)$$

$$F_\gamma = \gamma \pi L_1 \sin(\psi - \theta) \quad (S12)$$

$$F_D = \frac{\pi}{4} D^2 C_D \frac{\rho_l u_b^2}{2} \quad (S13)$$

where D is the diameter of the bubble, ρ_l is the density of the functional liquid, g is the gravity constant, ρ_g is the density of air, u_g is the velocity

of the gas across the pore, L is the pore size of the DPM, V_b is the bubble volume, C_{MC} is the added mass coefficient, t is time, γ is the surface tension of the functional liquid, θ is Young's CA, ψ is the texture angle, C_D is the drag coefficient of a bubble moving through an infinite liquid phase, u_b is the velocity of the bubble centre and $L_1 = L + 2R(1 - \sin \psi)$ is the diameter of the bubble contact with the substrate (Fig. 3b). Accordingly, the force balance equation of the submerged bubble is

$$F_B + F_M = F_I + F_\gamma + F_D \quad (S14)$$

If the air flow rate in this system is Q , the velocity of the gas across the pore is $u_g = 4Q/(\pi L^2)$ and the velocity of the bubble centre is $u_b = Q/(\pi D^2)$. Under the present experimental conditions, the magnitudes of the above forces are calculated and compared as $F_I \ll F_B$ and $F_M \ll F_B$. At a low flow rate, the viscous force is negligible during the growth of the bubble^{38,39}, $F_D \ll F_B$. Considering the insignificant effect of the density of air, equation S14 can be simplified as

$$\frac{1}{6}\pi D^3 \rho_g g = \gamma \pi L_1 \sin(\psi - \theta) \quad (S15)$$

Thus, the bubble detaches from the substrate when it reaches the maximum diameter D_{\max} , where

$$D_{\max} = \left(\frac{6\gamma}{\rho g} L_1 \sin(\psi - \theta) \right)^{\frac{1}{3}} \quad (S16)$$

The heterogeneity of the pore structure in the matrix will affect the formation process of the bubbles and further lead to the heterogeneity of the bubble diameter. In addition, owing to the hysteresis of the movement of the three-phase contact line during bubble formation, the maximum surface tension force cannot be reached. Thus, our controllable range of bubble diameter (D_{expt}) values is between D_{\max} and D_{\min} (Extended Data Fig. 5d).

The motion of PM in the rising bubbles

The motion of PM in the rising bubbles is influenced by several different mechanisms, including convection, gravitational deposition, inertial impaction and Brownian motion^{20,40,41}. The order of magnitude of the bubble Reynolds number is defined as $Re = 2U_b R_b / v_L$ (where U_b is the rising speed of the bubbles, R_b is the bubble radius and v_L is the kinematic viscosity of the functional liquids)⁴⁰, and the range of Re number is estimated to be approximately 10–100. The bubbles remain spherical and the shape oscillation is negligible, so the particle motion caused by convection can be ignored⁴². In addition, gravitational deposition is insignificant, because even for PM with a radius of 10 μm, as the gravity of PM is several orders of magnitude smaller than the viscous resistance, $F_D = 6\pi R_p v \eta$ (where v is the velocity of the particle and η is the gas viscosity; even for large-sized PM with $R_p = 10$ μm and small particle velocity $v = 1$ m s⁻¹, the viscous resistance $F_D = 3.37 \times 10^{-9}$ N, which is much larger than the particle gravity $G = 4.10 \times 10^{-11}$ N).

The dominance of particle inertial impaction and Brownian motion depends on the size of the particle. The motion state of suspended PM in the fluid flow can be described by the Stokes number $Stk = v_0 t / l$, where l is the characteristic dimension of the bubble. PM is subjected to viscous resistance during inertial motion, and its relaxation time is²⁰:

$$\tau = \frac{m}{f} = \frac{2\rho_p R_p^2}{9\eta} \quad (S17)$$

which represents the time required for the initial velocity v_0 of the particle to decrease to $v = v_0 e^{-1}$ because of the viscous resistance of the gas, m is the mass of the PM and $f = 6\pi\eta R_p$ is the drag coefficient of the aerosol. The calculated relaxation time for PM of different radii

Article

is listed in Extended Data Table 1. It can be found that the relaxation time of the PM of all sizes is much shorter than the time required for the bubble to rise until it bursts, $t_B = h/v_B$ (where v_B is the velocity of bubble rise; for bubble diameters of $D = 620 \mu\text{m}$ and $350 \mu\text{m}$, the corresponding velocities are about 0.1 m s^{-1} and 0.032 m s^{-1} , respectively, from the high-speed video), which indicates that the PM have sufficient time to inertially move in the bubble.

The distance that the particles travel at the initial velocity v_0 and within the relaxation time is called the stopping distance⁴³: $x_s = v_0 t$. Through experimental observation and calculation, the average initial velocity of the PM is $v_0 \approx 80 \text{ m s}^{-1}$, and the stopping distance x_s can then be calculated, as shown in Extended Data Table 1. When $R_p \geq 0.6 \mu\text{m}$, the particle's stopping distance $x_s \geq D$ ($D = 350 \mu\text{m}$). Therefore, because of the inertial impaction mechanism, the PM of $R_p \geq 0.6 \mu\text{m}$ will definitely be adsorbed to the gas–liquid interface (Fig. 3d).

For PM with $R_p < 0.6 \mu\text{m}$, Brownian motion becomes important as the particle size gradually decreases. The mean displacement Δx of the PM in Brownian motion can be given by Einstein's theory⁴³:

$$\begin{cases} \Delta x = \sqrt{\frac{4D_i t}{\pi}} \\ D_i = \frac{k_B T C}{6\pi\eta R_p} \end{cases} \quad (\text{S18})$$

where D_i is the diffusion coefficient, t is the time of particle movement, T is the absolute temperature and C is the Cunningham correction factor. Considering the fact that the maximum movement time of the particle is $t_{\max} = t_B = 1.875 \text{ s}$ (where $h = 60 \text{ mm}$ and $v_B \approx 0.032 \text{ m s}^{-1}$), the mean displacement can then be given. It can be seen from Extended Data Table 2 that only when $R_p = 0.005 \mu\text{m}$ are the mean displacement of the PM and the bubble size of the same order of magnitude. The small particles are also likely to be adsorbed to the gas–liquid interface in t_B owing to Brownian motion. According to the above discussion, it can be seen that for the particle with radius in the range $0.005 \mu\text{m} < R < 0.6 \mu\text{m}$, its motion is not dominated by inertial motion or Brownian motion but rather is formed by their competition. After the particle experiences the initial inertial action, it will still follow Brownian motion in the bubble. As the distance between the initial position and the adsorption position of the particles is often smaller than the diameter of the bubble, these particles still have a high probability to reach the gas–liquid interface. It is worth noting that when the particle radius is of a magnitude of ten nanometres, there is a trough of adsorption capacity. This is one of the reasons why the theoretical adsorption efficiency of our system cannot reach 100%. However, in practice, the particles with radii in the range $0.005 \mu\text{m} < R < 0.6 \mu\text{m}$ will also move inside the microbubble with the air flow when the thickness of the functional liquid is increased, which will further increase the probability of contacting the gas–liquid interface.

Adhesion of a single particle to the gas–liquid interface

In brief, when a single particle of radius R_p adheres to a gas bubble interface with a finite radius R_b , the surface free energy change (ΔG) of the particle, gas and liquid at the particle–gas–liquid interface can be described as $\Delta G = \gamma_{s-l} - \gamma_s - \gamma_l = -\gamma_l(\cos\theta + 1)$, where γ_{s-l} , γ_s and γ_l are the surface tension of the solid–liquid interface, solid and liquid, respectively, and θ is the CA between the liquid and the particle. According to the energy function, when $\theta \leq 180^\circ$, the adhesion of the particle to the gas–liquid interface can occur spontaneously, that is, the particle can be trapped by the liquid. Therefore, almost all particles will be captured by the liquid because very few solids have a CA of 180° (ref. ⁴⁴). When the particle is immersed inside the liquid, the energy change is $\Delta G = \gamma_{s-l} - \gamma_s - \gamma_{g-l}\cos\theta$. Hence, when $\theta \leq 90^\circ$, the immersion of the particle in the liquid can occur spontaneously and the particle can be absorbed by the liquid.

Other forces on the particle include the force resulting from the capillary pressure inside the gas bubble (F_p), the buoyancy force (F_B), the gravitational force (F_G) and the surface tension force of the liquid (F_γ) (Fig. 3e and Extended Data Fig. 6b). Under static conditions, the equation describing the equilibrium forces of a single particle is given by¹¹:

$$F_p - F_G + F_B - F_\gamma = 0 \quad (\text{S19})$$

The forces are expressed as follows:

$$F_p = \frac{2\gamma_l}{R_b} \cdot \pi(R_p \sin\varphi)^2 \quad (\text{S20})$$

$$F_G = \frac{4\pi R_p^3 \rho_s g}{3} \quad (\text{S21})$$

$$F_B = \frac{\pi R_p^3}{3} (1 - \cos\varphi)^2 (2 + \cos\varphi) \rho_l g \quad (\text{S22})$$

$$F_\gamma = \gamma_l \cdot 2\pi R_p \sin\varphi \cdot \sin(\varphi + \theta - \pi) \quad (\text{S23})$$

where φ is the penetration angle, ρ_s is the solid density, ρ_l is the liquid density and g is the gravity constant. For a dynamic process, when the penetration angle φ is varying, the forces defined above may not be in equilibrium. In addition, the gravitational and buoyancy forces of the particle are ignored here because they are negligible compared to the surface tension force. The capture force F_c is defined as the resultant force acting downwards:

$$F_c = F_p - F_\gamma \quad (\text{S24})$$

When $F_c = 0$, $\varphi = \pi - \theta + \arcsin\left(\frac{R_p \sin\varphi}{R_b}\right)$ and $\varphi \approx \pi - \theta$. Hence, when $\theta > 90^\circ$ and $\varphi < 90^\circ$, most of the volume of the particle is in the gas side (Extended Data Fig. 6b). When $\theta < 90^\circ$ and $\varphi > 90^\circ$, corresponding to when the penetration angle φ is increasing, the particle ultimately detaches from the gas–liquid interface and moves into the liquid (Fig. 3e).

In addition, the adsorption energy W of particles at the interface can be expressed as²² $W = \gamma_0 R_p^2 \pi (1 + \cos\theta)^2$, where γ_0 is the interfacial tension and R_p is the particle radius. From the equation, it can be found that the adsorption energy increases significantly when the CA is less than 180° , for example, the adsorption energy is about $1 \times 10^6 k_B T$ if the radius of the particles is $1 \mu\text{m}$ and the CA is 150° , which shows that the particles, even super-hydrophobic particles, will be strongly held in the interface⁴⁵. Moreover, the adsorption energy is also closely related to the particle size⁴⁶, and the interface adsorption energy of intermediate wettability particles ($\theta = 90^\circ$) with radii of $0.1 \mu\text{m}$ would be about $10^6 k_B T$. In our system, the size of soot particles is generally greater than $0.1 \mu\text{m}$, so when the particles are adsorbed to the gas–liquid interface, it is difficult for the particles to desorb from the bubble and move to the gas surface owing to their strong adsorption energy. Therefore, both hydrophobic and hydrophilic particles can be captured by the functional liquid in the ELBS.

Derivation of the purification efficiency of the ELBS

The number of adsorbed particles is affected by two factors, one in the bubble-forming process (filtration) and the other in the bubble-rising process (absorption). There are three particle absorption mechanisms: inertia, sedimentation and diffusion²⁰. Absorption coefficients corresponding to the above mechanisms are influenced by several factors, such as the rising velocity of the bubble, the radius of the bubble, the relaxation time of the particle, the density and the radius of the particle. In the experiments, most of the parameters are approximatively constant in one purification process, such as the rising velocity and

the radius of the bubble. It is assumed that the size of the particles is an average value so that we can simplify the model and get that the total absorption coefficient, which is a constant. Here we derive the change of particle mass concentration within a single bubble in the bubble-rising process.

We define the particle mass concentration as $c = W/V$, or $c_t = \delta W_t / \delta V_t$, where W is the mass of the particles in a single bubble with volume V . In the particle absorption process it is hypothesized that the amount of absorption Γ crossing a unit area in unit time of the PM is proportional to the concentration c_t of the PM, namely $\Gamma_t = k c_t$, where k is the total absorption coefficient. Thus, in the bubble-rising process, the change of particle number within time dt can be expressed as

$$dW = -\pi D^2 \Gamma dt = -6kD^{-1}W dt \quad (\text{S25})$$

where D is the bubble diameter. When the bubble begins to rise, the mass of particle in the bubble is given as $W_0 - \Delta W_1$, where W_0 is the initial amount of particle in the gas within a single bubble volume and ΔW_1 is the decrease in the bubble-forming process. After the bubble detaches from the PPy matrix, it rises rapidly with a uniform velocity V_b and the rising time Δt_2 is

$$\Delta t_2 = \frac{h}{V_b} \quad (\text{S26})$$

where h is the thickness of the functional liquid and the velocity V_b is suggested by Wallis⁴⁷ for a Re range values of approximately $1 < \text{Re} < 100$ to be

$$V_b = 0.14425 g^{5/6} \left(\frac{\rho_l}{\mu_l} \right)^{2/3} D^{3/2} \quad (\text{S27})$$

where μ_l is the viscosity of the functional liquid.

According to equation S26, the total absorption in the rising process can be derived as

$$\Delta W_2 = (W_0 - \Delta W_1) \left[1 - \exp \left(-41.59 \frac{\mu_l^{2/3}}{g^{5/6} \rho_l^{2/3}} k \frac{h}{D^{5/2}} \right) \right] \quad (\text{S28})$$

Thus, the total particle absorption efficiency is

$$\eta = \frac{\Delta W_1 + \Delta W_2}{W_0} = 1 - \left(1 - \frac{\Delta W_1}{W_0} \right) \exp \left(-41.59 \frac{\mu_l^{2/3}}{g^{5/6} \rho_l^{2/3}} k \frac{h}{D^{5/2}} \right) \quad (\text{S29})$$

Data availability

The data that support the findings of this study are available from the corresponding author.

31. Liu, M., Nie, F. Q., Wei, Z., Song, Y. & Jiang, L. In situ electrochemical switching of wetting state of oil droplet on conducting polymer films. *Langmuir* **26**, 3993–3997 (2010).
32. Young, T. An essay on the cohesion of fluids. *Philos. Trans. R. Soc. London* **95**, 65–87 (1805).
33. Owens, D. K. & Wendt, R. C. Estimation of the surface free energy of polymers. *J. Appl. Polym. Sci.* **13**, 1741–1747 (1969).
34. Kape, A., Ruick, B. & Drusch, S. Characterisation of the work of adhesion of food grade coating materials on a maltodextrin model surface. *Chem. Eng. Res. Des.* **110**, 152–159 (2016).
35. Harris, A. F. & Beevers, A. The effects of grit-blasting on surface properties for adhesion. *Int. J. Adhes. Adhes.* **19**, 445–452 (1999).
36. Kwon, G. et al. On-demand separation of oil-water mixtures. *Adv. Mater.* **24**, 3666–3671 (2012).
37. Liu, C. J., Liang, B., Tang, S. W. & Min, E. Z. Effects of orifice orientation and gas-liquid flow pattern on initial bubble size. *Chin. J. Chem. Eng.* **21**, 1206–1215 (2013).
38. Longuet-Higgins, M. S., Kerman, B. R. & Lunde, K. The release of air bubbles from an underwater nozzle. *J. Fluid Mech.* **230**, 365–390 (1991).
39. Higuera, F. J. Injection and coalescence of bubbles in a very viscous liquid. *J. Fluid Mech.* **530**, 369–378 (2005).
40. Ghiaasiaan, S. M. & Yao, G. F. A theoretical model for deposition of aerosols in rising spherical bubbles due to diffusion, convection, and inertia. *Aerosol Sci. Technol.* **26**, 141–153 (1997).
41. Charvet, A., Bardin-Monnier, N. & Thomas, D. Can bubble columns be an alternative to fibrous filters for nanoparticles collection? *J. Hazard. Mater.* **195**, 432–439 (2011).
42. Ghiaasiaan, S. M. & Yao, G. F. Diffusive and convective deposition of aerosols in rising spherical bubbles with internal circulation. *Int. J. Multiphase Flow* **21**, 907–918 (1995).
43. Licht, W. The movement of aerosol particles. *J. Soc. Cosmet. Chem.* **23**, 657–678 (1972).
44. Larmour, I. A., Bell, S. E. & Saunders, G. C. Remarkably simple fabrication of superhydrophobic surfaces using electroless galvanic deposition. *Angew. Chem. Int. Ed.* **46**, 1710–1712 (2007).
45. Liu, M., Wang, S. & Jiang, L. Nature-inspired superwettability systems. *Nat. Rev. Mater.* **2**, 17036 (2017).
46. Binks, B. P. Particles as surfactants – similarities and differences. *Curr. Opin. Colloid Interface Sci.* **7**, 21–41 (2002).
47. Wallis, G. B. The terminal speed of single drops or bubbles in an infinite medium. *Int. J. Multiphase Flow* **1**, 491–511 (1974).
48. Tan, K. L., Tan, B. T. G., Kang, E. T. & Neoh, K. G. The chemical nature of the nitrogens in polypyrrole and polyaniline: a comparative study by x-ray photoelectron-spectroscopy. *J. Chem. Phys.* **94**, 5382–5388 (1991).
49. Tan, X., Hu, C., Zhu, Z., Liu, H. & Qu, J. Electrically pore-size-tunable polypyrrole membrane for antifouling and selective separation. *Adv. Funct. Mater.* **29**, 1903081 (2019).
50. Zhang, H. et al. Design of three-dimensional gradient nonwoven composites with robust dust holding capacity for air filtration. *J. Appl. Polym. Sci.* **136**, 47827 (2019).
51. Liu, J. et al. Low resistance bicomponent spunbond materials for fresh air filtration with ultra-high dust holding capacity. *RSC Adv.* **7**, 43879–43887 (2017).
52. Liu, J. et al. Polyethylene/polypropylene bicomponent spunbond air filtration materials containing magnesium stearate for efficient fine particle capture. *ACS Appl. Mater. Interfaces* **11**, 40592–40601 (2019).
53. Liu, B., Zhang, S., Wang, X., Yu, J. & Ding, B. Efficient and reusable polyamide-56 nanofiber/nets membrane with bimodal structures for air filtration. *J. Colloid Interface Sci.* **457**, 203–211 (2015).
54. Li, Y. Y. et al. Semi-interpenetrating polymer network biomimetic structure enables superelastic and thermostable nanofibrous aerogels for cascade filtration of PM2.5. *Adv. Funct. Mater.* **30**, 1910426 (2020).

Acknowledgements This work was supported by the National Natural Science Foundation of China (grant nos. 52025132, 21975209, 21621091, 22021001 and 22121001), the National Key R&D Programme of China (grant no. 2018YFA0209500), the 111 Project (grant nos. B17027 and B16029) and the Science and Technology Projects of Innovation Laboratory for Sciences and Technologies of Energy Materials of Fujian Province (grant no. RD2022070601). We thank L. Huang, L. Min, B. Chen, H. Liu, D. Wu and K. Zhan for their support and discussion of the synthesis and measurements of the materials.

Author contributions X.H. conceived the project and designed the research. Y.Z. and S.W. synthesized the materials. Y.Z., Y. Han, Z.S., Y. Hou, C.W. and M.W. prepared and characterized the samples, and analysed the data. Y.Z., L.Q. and Y. Han performed the pressure, microbubble size and air purification experiments and analysed the data. Y.Z., X.J., D.Z., Z.S. and L.Q. built the mathematical model. Y.Z., X.C. and X.H. wrote the manuscript. All the authors contributed to the data analysis, discussion and manuscript preparation.

Competing interests The authors declare no competing interests.

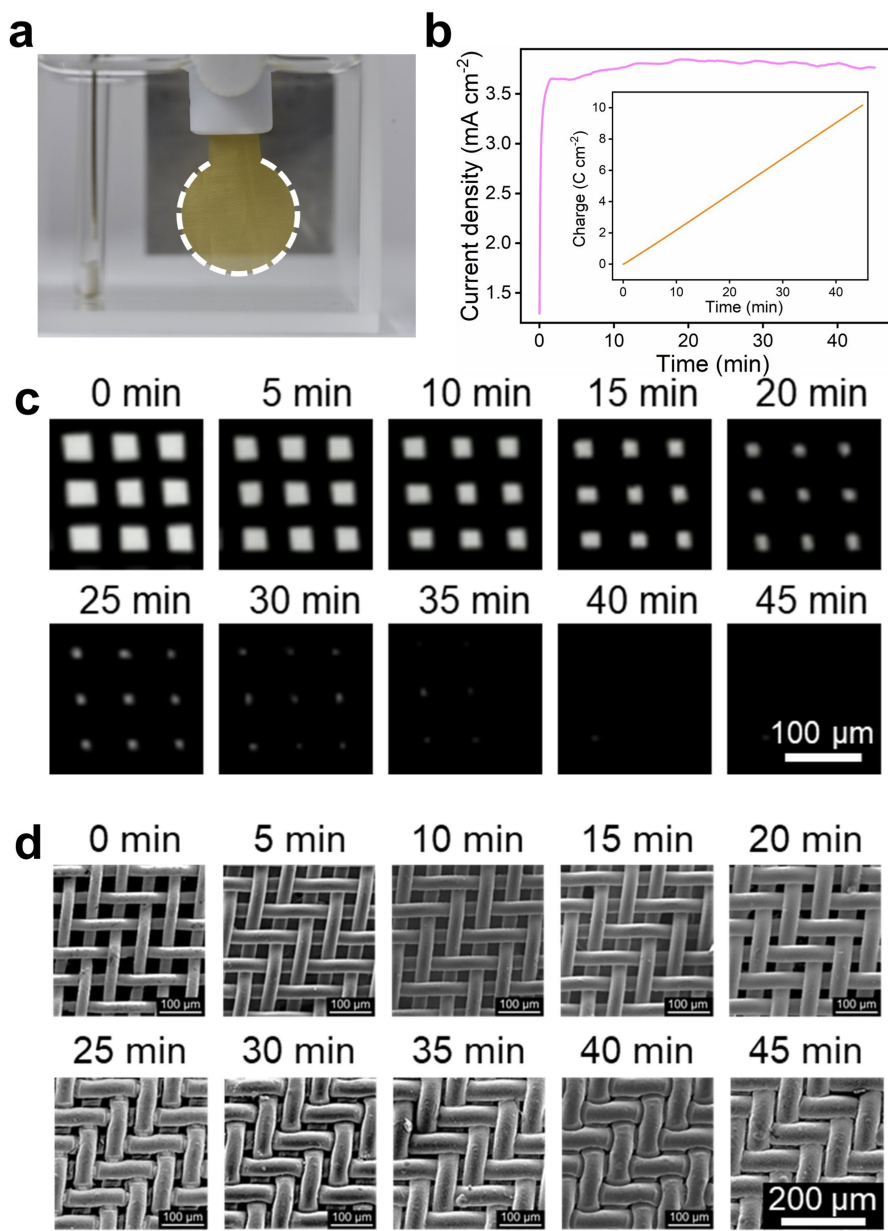
Additional information

Supplementary information The online version contains supplementary material available at <https://doi.org/10.1038/s41586-022-05124-y>.

Correspondence and requests for materials should be addressed to Xu Hou.

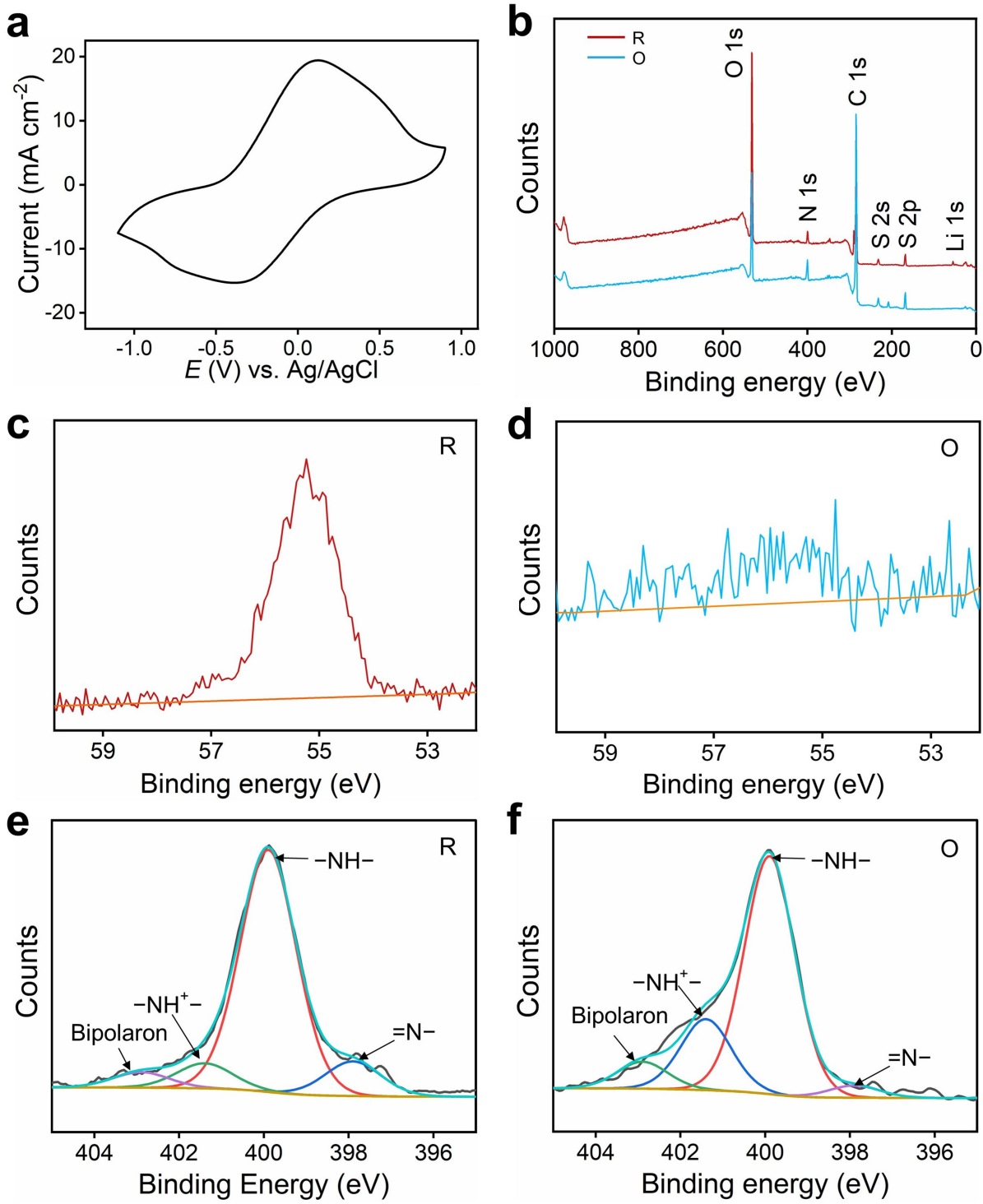
Peer review information *Nature* thanks Pascal Guiraud and the other, anonymous, reviewer(s) for their contribution to the peer review of this work.

Reprints and permissions information is available at <http://www.nature.com/reprints>.



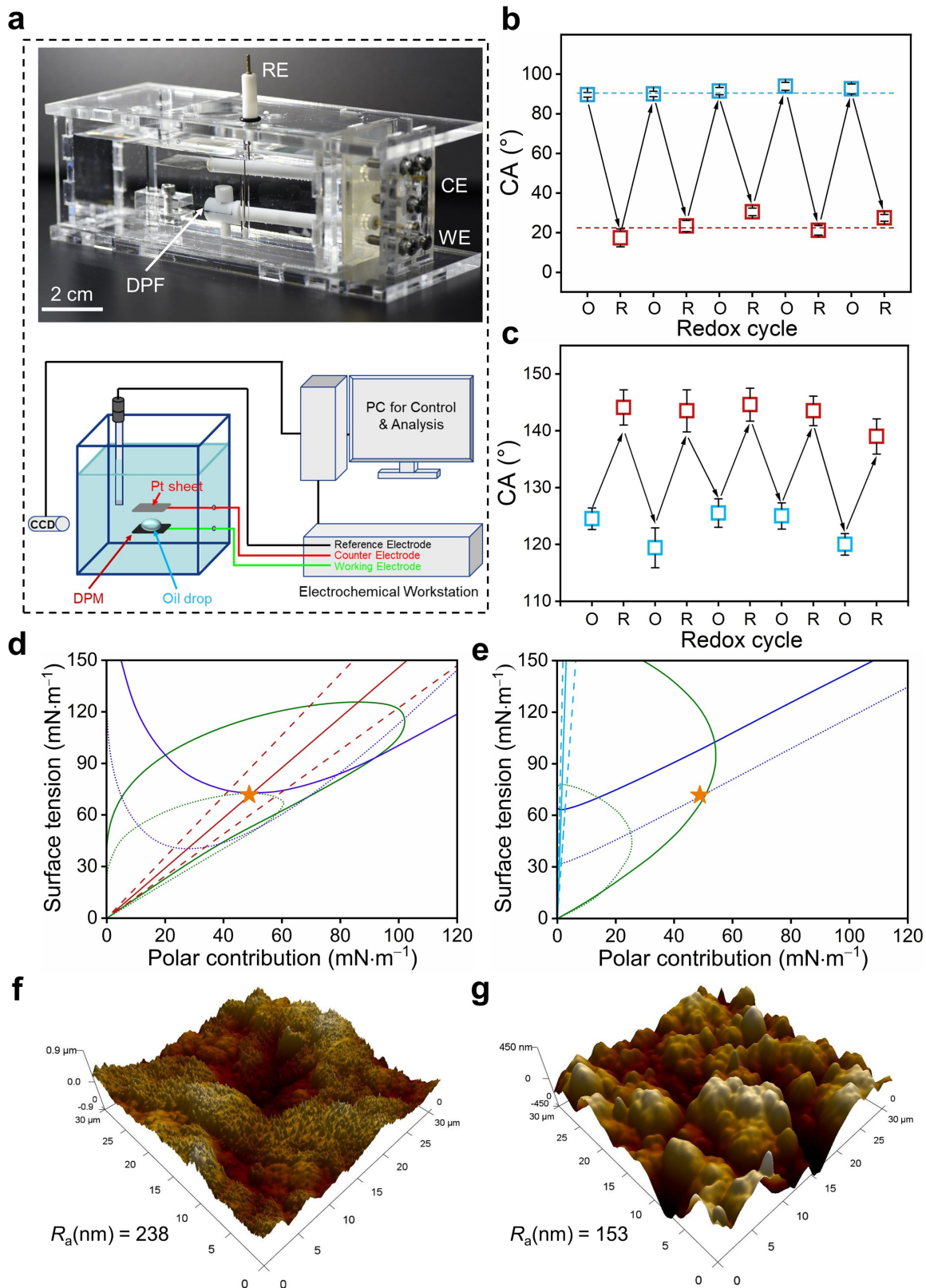
Extended Data Fig. 1 | The electrochemical polymerization of doped PPy.
a. The photo of the electrochemical polymerization setup. **b.** Current density dependent electrochemical polymerization time. Inset: Charge density

dependent electrochemical polymerization time. **c.** The optical images of doped PPy coated SSM at different polymerization times. **d.** SEM images of doped PPy coated SSM at different polymerization times.



Extended Data Fig. 2 | The surface composition analysis of DPM in the redox process. **a.** Cyclic voltammetry (CV) curve of DPM in 0.1 M LiClO_4 at a scan rate of 50 mV s^{-1} . The curve shows the reversibility of the redox process with an oxidation peak at 0.12 V and a reduction peak at -0.39 V . **b.** The X-ray photoelectron spectroscopy (XPS) survey scans of DPM in different states, which prove the matrix surface composition changes in the redox process. **c, d.** High-resolution Li 1s XPS spectra of DPM in the reduction state (c) and the

oxidation state (d), which show the Li^+ ions doping and dedoping during the redox processes. **e, f.** High-resolution N 1s XPS spectra of DPM in the reduction state (e) and the oxidation state (f). Four types of nitrogen environments are present in DPM. The higher peaks at 401.4 eV and 402.9 eV can be assigned to the positively charged $-\text{HN}^+$ - and bipolarons moieties⁴⁸. The positively charged N moieties are higher in the oxidation state, which indicates that the redox reaction have occurred on the DPM.



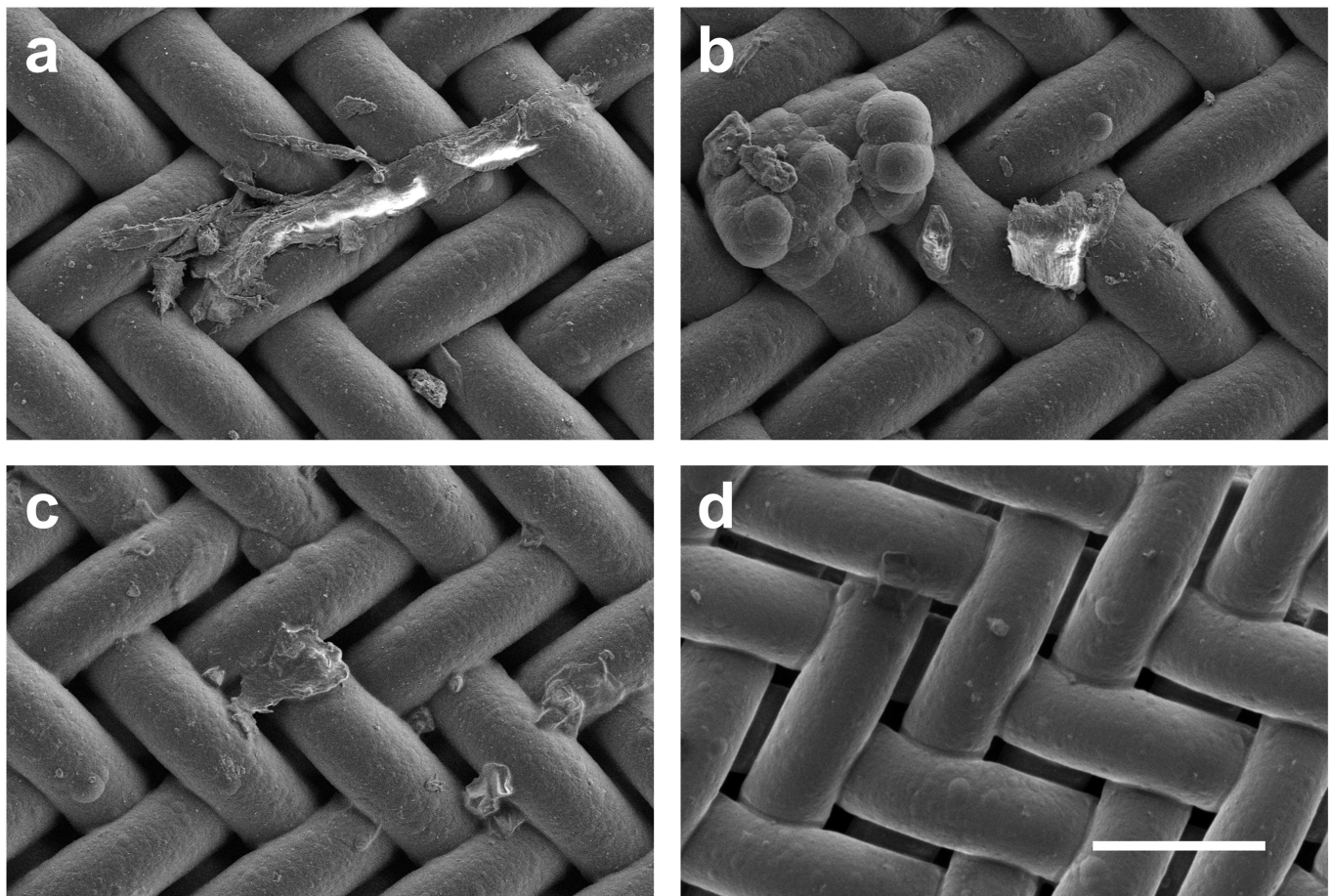
Extended Data Fig. 3 | See next page for caption.

Extended Data Fig. 3 | The wettability and morphology of the DPF in the redox process.

a. The self-designed setup for in situ monitoring the contact angle of a dichloromethane droplet on the DPF during adjusting the electrochemical potentials underwater. A three-electrode system was used to control the electrochemical potential. DPF was served as the working electrode. Ag/AgCl electrode and a platinum plate were used as the reference electrode and the counter electrode, respectively. 0.1 M LiClO₄ aqueous solution was used as the electrolyte. **b.** Reversible wettability switching of the functional liquid on DPF during the continuous cycle redox process. To obtain a wide range of wettability values with a small potential difference, we selected +0.40 V and -0.60 V as the optimal working oxidation and reduction potentials, respectively, based on the contact angle analysis at different potentials in Fig. 2b. Error bars represent the standard deviation from five independent measurements. **c.** Underwater wettability switching of oil on DPF during the cycle redox process. Error bars represent the standard deviation from five

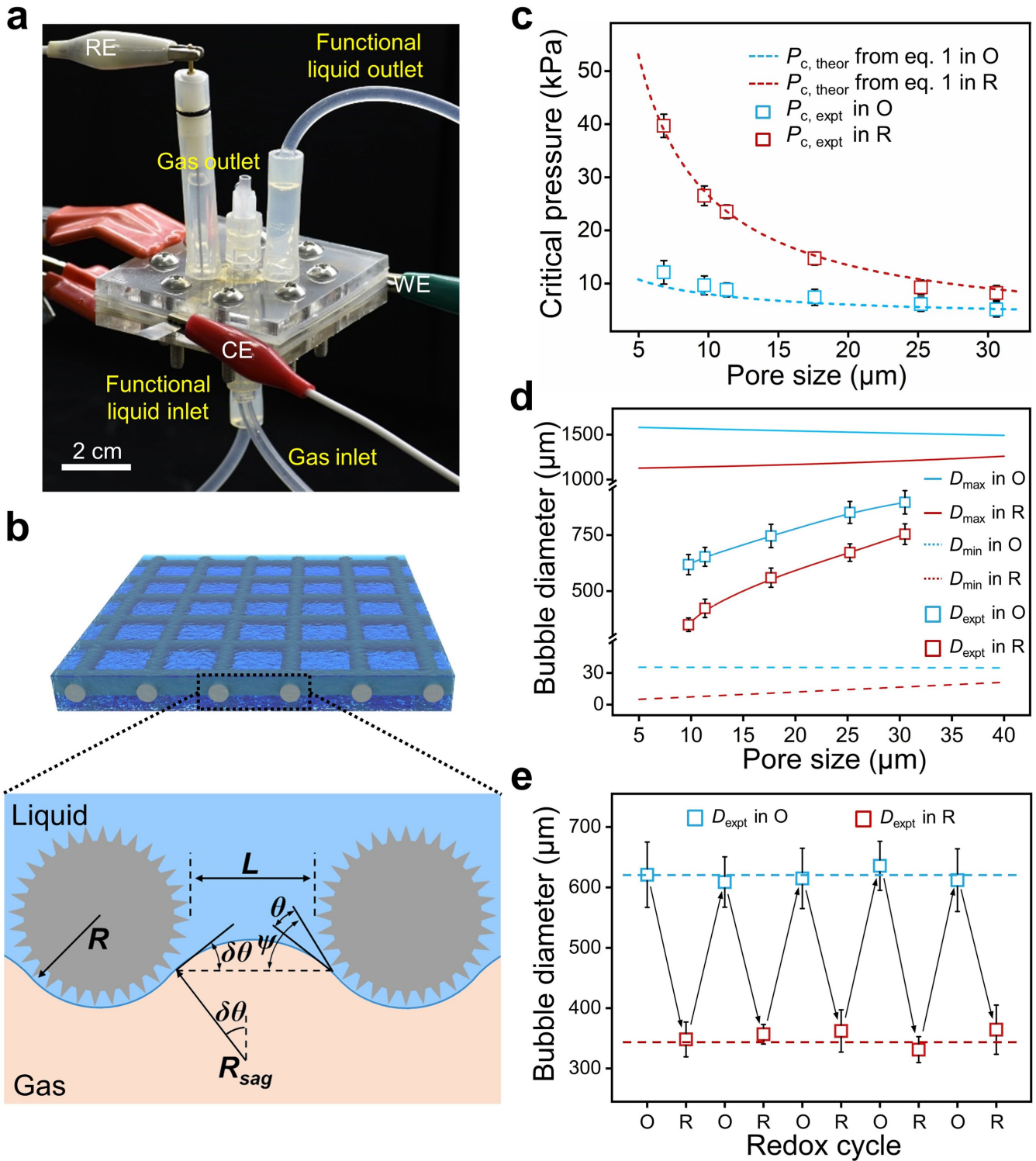
independent measurements. **d, e.** Analysis of the adhesion work between the functional liquid and the matrix in reduction state (d) and oxidation state (e): the polar part of the surface tension/energy and the corresponding surface tension/energy can be identified and the combination of them provides the optimum adhesion between DPF and functional liquid. The blue and red straight line represents the optimum adhesive force, and a range of acceptable performance can be proposed. From the results, one can conclude that the functional liquid falls in the optimum zone in the reduction state, which indicates that the affinity between the functional liquid and the matrix adheres well. **f, g.** 3D atomic force microscope (AFM) images show height variations on the surface of the matrix in reduction state (f) and oxidation state (g). AFM results suggest that the surface of the matrix changes from smooth to rough during the reduction process due to the influx of lithium ions⁴⁹, which could also increase the hydrophilicity of the surface.

Article



Extended Data Fig. 4 | The SEM images of the filtrated DPM after backwashing. **a**, DPM in oxidation state without liquid-lining; **b**, DPM from ELBS in oxidation state with liquid-lining; **c**, DPM in reduction state without liquid-lining; **d**, DPM from ELBS in reduction state with liquid-lining; Scale bar, 100 μm . After the backwashing, we can find that few particles exist on the liquid-lined matrix while many particles exist on the matrix without liquid, which demonstrate that the liquid-lining improves the anti-fouling property of the matrix. In addition, we can use the functional liquid to regulate the wettability of the matrix, which will influence the affinity among the

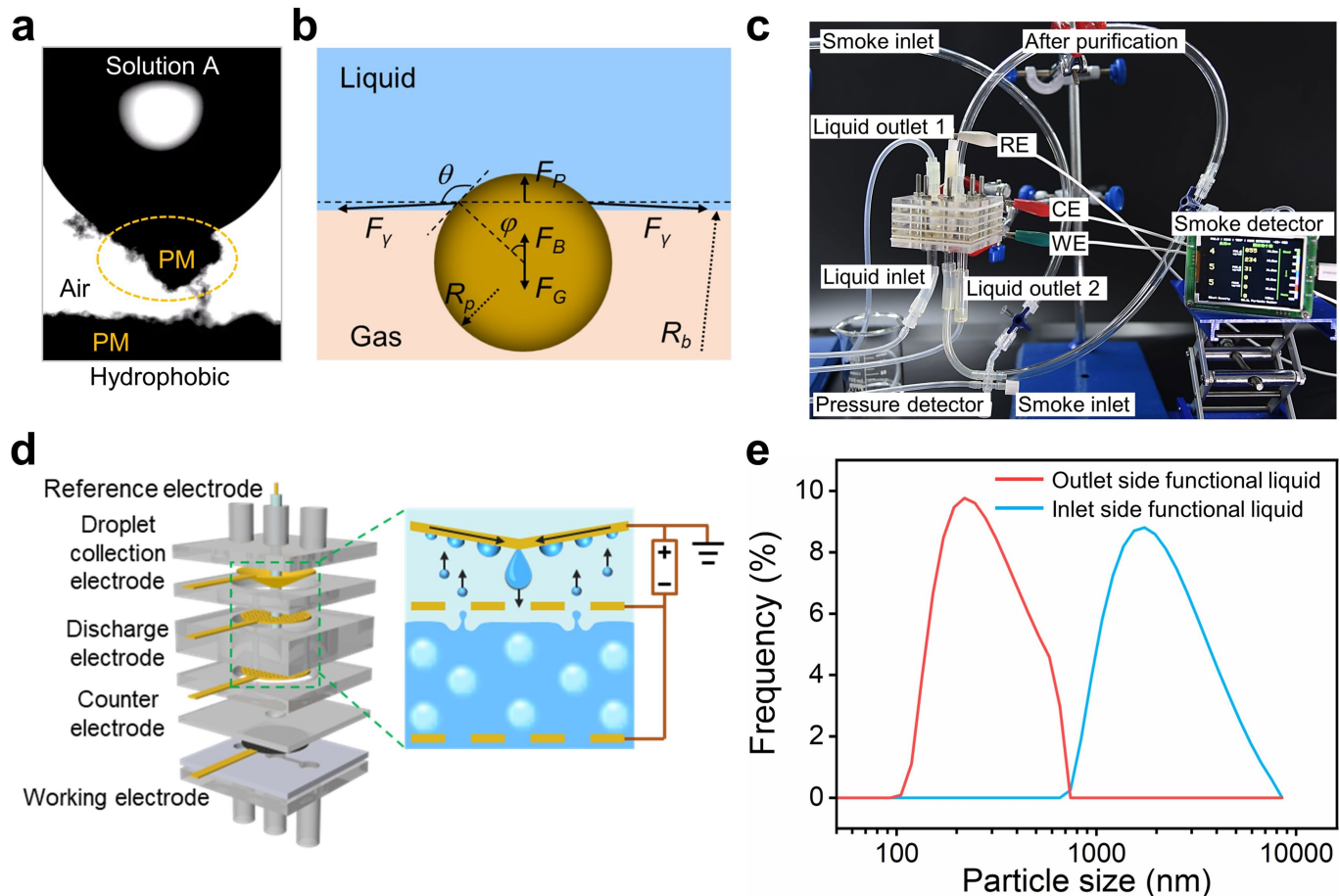
contaminant, functional liquid, and matrix and further prevent particle accumulation. The surface of the matrix with liquid-lining in reduction state was cleaner than that in oxidation state, because of the stronger affinity between the lined liquid and the reduction state matrix. Therefore, we can apply different potentials to change the wettability of the matrix to reduce the affinity to further prevent particles accumulation. In addition, once the regulation is completed, the redox state of the liquid-based matrix can be maintained all the time without continuous power input.



Extended Data Fig. 5 | Transport properties and microbubbles generation of ELBS. **a.** Optical image of the pressure measurement setup. **b.** Schematic of the pressure-induced bulge of the liquid-air interface. Here, L is the pore size of DPM, R is the radius of the cylindrical fiber in DPM, R_{sag} is the critical radius of curvature of the liquid-air interface, θ is Young's contact angle, ψ is the texture angle, $\delta\theta$ is the convex angle. **c.** Theoretical and experimental value of critical pressure (P_c) of air passing through ELBS with different pore size matrices during the redox process. The error bars represent the standard deviation from five independent measurements. **d.** The theoretical maximum and minimum and experimental diameters of microbubbles generated from ELBS with different matrix pore sizes in the redox process. Error bars represent the standard deviation from five independent measurements. **e.** The sizes of the microbubbles generated from ELBS with the average pore size of ~9.7 μm in the repeating redox process. Error bars represent the standard deviation from ten independent bubble measurements.

five independent measurements. **d.** The theoretical maximum and minimum and experimental diameters of microbubbles generated from ELBS with different matrix pore sizes in the redox process. Error bars represent the standard deviation from five independent measurements. **e.** The sizes of the microbubbles generated from ELBS with the average pore size of ~9.7 μm in the repeating redox process. Error bars represent the standard deviation from ten independent bubble measurements.

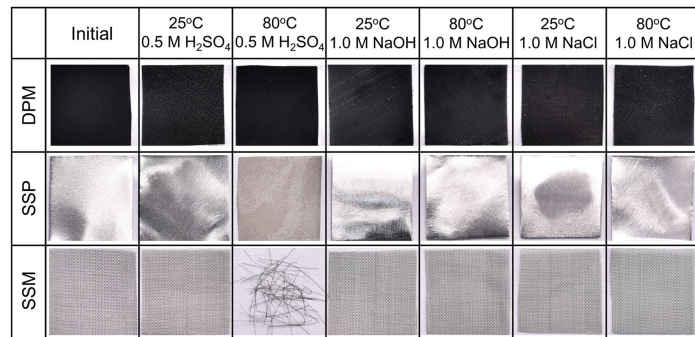
Article



Extended Data Fig. 6 | The air purification performance of the ELBS.

a. Adhesion of the hydrophobic particles to the gas–liquid interface. **b.** Representation of the forces acting on the hydrophobic particle at the bubble interface. Here, R_p is the radius of the particle, R_b is the radius of the bubble, F_p is the force resulting from the capillary pressure inside the gas bubble, F_b is the buoyancy force, F_g is the gravitational force, F_γ is the surface tension force of the liquid. **c.** Optical image of the in situ study customized particulate matter

(PM) purification system. **d.** The schematic of the purification system and the capture process of the droplets generated from the bursting bubbles. **e.** The particle size distribution in the liquid in the inlet side and outlet side. There are two purification steps: the direct interception and removal of larger PM in the polluted air by the liquid-lined porous matrix (inlet side), and the capture of smaller PM by the functional liquid through the microbubble interface (outlet side).



Extended Data Fig. 7 | Optical photographs of DPM, SSP (stainless-steel plate), and SSM after immersed in 1.0 M NaOH solutions, 0.5 M H₂SO₄ solutions, 1.0 M NaCl solutions, at different temperatures for 24 h, respectively. Scale bar, 1 cm.

Article

Extended Data Table 1 | Inertial impaction of particles with different radius

R_p (μm)	τ (s)	x_s (m)	Stk (dimensionless)
5	3.10×10^{-4}	2.48×10^{-2}	40
0.8	7.93×10^{-6}	6.34×10^{-4}	1.02
0.6	4.46×10^{-6}	3.57×10^{-4}	0.5
0.5	3.10×10^{-6}	2.48×10^{-4}	0.4
0.05	3.10×10^{-8}	2.48×10^{-6}	4×10^{-3}

Extended Data Table 2 | Brownian diffusion of particles with different radius

R_p (μm)	D ($\text{m}^2 \text{s}^{-1}$)	Δx (m)
0.5	2.74×10^{-11}	8.09×10^{-6}
0.05	6.82×10^{-10}	4.04×10^{-5}
0.005	5.24×10^{-8}	3.54×10^{-4}

Article

Extended Data Table 3 | The purification efficiency of ELBS with different heights of the functional liquid in different states

Name	D (μm)	η % (mean (SD), $n = 5$)			
		$h = 60$ mm	$h = 40$ mm	$h = 20$ mm	$h = 3$ mm
Working state	350	99.6 (0.8)	98.6 (0.6)	95.5 (1.2)	82.9 (2.5)
Initial state	618	87.9 (2.5)	85.6 (1.6)	81.5 (1.5)	76.0 (2.2)

Extended Data Table 4 | Comparison of the purification performance between ELBS prepared in this work and other current filtration media^{7,50-54}

Materials	Efficiency (%)	Dust holding capacity (g m ⁻²)	Pressure drop (Pa) (define dust holding capacity; compared with the initial pressure drop)	Reference
Gold Frame 94	94	165	95 (125-30)	7
Gold Frame 82	82	119	105 (125-20)	7
Multilayer filter (N*3/M*2)	99.52	23.5	273.74	50
Bicomponent spunbond materials (BCS)	97.02	9.36	964.86 (1000-35.14)	51
BCS PE/PP-M-0.6	98.94	10.87	962.08 (1000-37.92)	52
PA-56 NFN	99.995	49	889 (1000-111)	53
IPNFAs	99.98	114	422	54
Melt-blown filter	98.1	122	185	This work
ELBS (O)	87.9	840	185	This work
ELBS (R)	99.6	950	185	This work